SYNTHESIS AND CHARACTERISATION OF GEOPOLYMERS FROM GGBS ACTIVATED BY DIATOMACEOUS EARTH AND RICE HUSK ASH

M.Tech. Thesis

By

Manish Kumar Chaudhary

(2302104003)

DEPARTMENT OF CIVIL ENGINEERING

INDIAN INSTITUTE OF TECHNOLOGY INDORE

MAY 2025

SYNTHESIS AND CHARACTERISATION OF GEOPOLYMERS FROM GGBS ACTIVATED BY DIATOMACEOUS EARTH AND RICE HUSK ASH

A THESIS
Submitted in partial fulfilment of the academic
requirements for the award of the degree
of
Master of Technology
(2023 – 2025)
In

Structural Engineering
By
Manish Kumar Chaudhary
(2302104003)
Guided By

Prof. Sandeep Chaudhary

(Professor)

DEPARTMENT OF CIVIL ENGINEERING
INDIAN INSTITUTE OF TECHNOLOGY INDORE
MAY 2025

INDIAN INSTITUTE OF TECHNOLOGY INDORE

CANDIDATE'S DECLARATION

I hereby certify that the work which is being presented in the thesis entitled **SYNTHESIS AND CHARACTERIZATION OF GEOPOLYMERS FROM GGBS ACTIVATED BY DIATOMACEOUS EARTH AND RICE HUSK ASH** in the partial fulfilment of the requirements for the award of the degree of **MASTER OF TECHNOLOGY** and submitted in the **Department of Civil Engineering, Indian Institute of Technology Indore**, is an authentic record of my own work carried out during the period from July 2024 to May 2025 under the supervision of Prof. Sandeep Chaudhary, Professor, Department of civil engineering, Indian Institute of Technology Indore.

The matter presented in this thesis has not been submitted by me for the award of any other degree of this or any other institute.

Manish 28/05/2025

Signature of the student with date
(MANISH KUMAR CHAUDHARY)

This is to certify that the above statement made by the candidate is correct to the best of my/our knowledge.

Signature of the Supervisor of M.Tech. Thesis (with date) SChaudhary
Prof. Sandeep Chaudhary 29.05.2025

Manish Kumar Chaudhary has successfully given his M.Tech. Oral Examination held on 9th May 2025.

SChaudhary

Signature of the Supervisor of M.Tech. Thesis
Date: 29.05.2025

Convener, DPGC
Date:

ACKNOWLEDGEMENTS

I would like to express my heartfelt gratitude to **Prof. Sandeep Chaudhary** for their unwavering support, invaluable expertise, and insightful guidance throughout this project. I am also deeply thankful to Habtamu Melesse, Dr. Sanchit Gupta, Gaurav Sharma, Akash Paradkar, Astha Sharma, and Dr. Ashita Singh**,** whose thoughtful suggestions and assistance were instrumental in helping me understand the complexities of the project. Their constant availability and the collaborative environment in the lab played a crucial role in fostering my interest in the work.

A special note of thanks to Ghanshyam Sir, Suresh Sir, and Rakesh Sir for their diligent equipment maintenance and ensuring that all instruments were in excellent working condition during the project.

I want to acknowledge the unwavering support of all my friends, whose friendship and positivity have been a great source of strength while working on this project.

I also thank my parents, elder brother, and sister for their constant, unconditional support.

Through the combined efforts and support of these individuals, I was able to grasp the project and successfully complete the experimental work fully. This report would not have been possible without their invaluable contributions.

Manish **28/05/2025**

Manish Kumar Chaudhary (2302104003)

Date: 28/05/2025

ABSTRACT

The two silica sources used to synthesise activating solutions for alkali-activating ground granulated blast-furnace slag (GGBS) were agricultural by-product rice husk ash (RHA) and naturally occurring sedimentary rock diatomaceous earth (DE), both rich in amorphous silica. Geopolymers were fabricated using a 10 M NaOH-based activating solution with RHA and DE at 0%, 5%, 10%, and 15%. Mechanical and durability properties were assessed through compressive strength, density, water absorption, and porosity testing, while microstructural examinations employed XRD, FTIR, and FESEM-EDS analyses. Results confirm that RHA and DE can independently substitute commercial sodium silicate as efficient silica sources, with optimal performance at 5% addition for both materials. The optimised mixes exhibited superior binder formation with the presence of amorphous calcium-alumino-silicate hydrate (C-A-S-H) gels and hydrotalcite-like phases, indicative of efficient alkali activation. The optimised mix with DE achieved a compressive strength of 34.85 MPa and a bulk density of 1.91 g/cm^3, while the RHA mix achieved 27.05 MPa and 1.92 g/cm^3, respectively. This study confirms the feasibility of using RHA and DE as alternative silica sources in geopolymer production, reducing costs and environmental impacts by lowering CO_2 emissions and eliminating the need for high-energy sodium silicate.

TABLE OF CONTENTS

LIST OF FIGURES

LIST OF TABLES

NOMENCLATURE

Symbol/Abbreviation	**Description**
GGBS/Slag	Ground Granulated Blast Furnace Slag
RHA/ DE	Rice Husk Ash/ Diatomaceous Earth
NaOH/ Na_2SiO_3	Sodium Hydroxide/ Sodium Silicate
NH	Control sample without RHA or DE
DE5, DE10, DE15	Geopolymer samples with 5%, 10%, and 15% DE (by wt. of GGBS)
RH5, RH10, RH15	Geopolymer samples with 5%, 10%, and 15% RHA (by wt. of GGBS)
C–A–S–H	Calcium–Alumino–Silicate–Hydrate gel
N–A–S–H	Sodium–Alumino–Silicate–Hydrate gel
C–(N)–A–S–H	Mixed calcium–sodium aluminosilicate hydrate gel
XRD/XRF	X-ray Diffraction/ X-ray Fluorescence
FTIR	Fourier Transform Infrared Spectroscopy
FESEM	Field Emission Scanning Electron Microscopy
EDS	Energy Dispersive X-ray Spectroscopy
L/S	Liquid-to-Solid ratio
IS 4031, IS516	Indian Standard code for cement testing
ASTM C642	Standard Test Method for Density, Absorption, and Voids.
ASTM C230	Standard Specification for Flow Table for Use in Tests of Cement
Na-A	Sodium Zeolite A (Linde Type A) $Na_{12}(AlO_2)_{12}(SiO_2)_{12}\cdot 27H_2O$
Na-P1	Sodium Zeolite P1 (Type P1) $Na_6Al_6Si_{10}O_{32}\cdot 12H_2O$

Hydrotalcite	Magnesium–Aluminium layered double hydroxide, $Mg_6Al_2(OH)_{16}CO_3 \cdot 4H_2O$
°C	Degree Celsius
cm^3	Cubic centimetre
wt.%	Weight percent

Chapter 1

INTRODUCTION

The construction industry is a major contributor to climate change and global sustainability challenges. In particular, Ordinary Portland Cement (OPC) production is a leading source of CO_2 emissions [1]. Each kilogram of OPC releases approximately 0.66–0.82 kg of CO_2 [1], with global production ranging from 3.5 to 4 billion tonnes annually [2]. Cumulatively, cement manufacturing accounts for roughly 5–7% of all anthropogenic CO_2 emissions [1]. These emissions primarily arise from the high-temperature calcination of limestone ($CaCO_3 \rightarrow CaO + CO_2$) and fuel combustion during clinker production [1, 2]. Consequently, reducing the carbon footprint of cementitious materials is critical for sustainable construction. Geopolymers have emerged as a promising alternative to OPC [3]. Introduced by Davidovits in 1978, geopolymers are inorganic polymers produced through the alkali activation of aluminosilicate precursors [3]. Unlike OPC, geopolymer binders eliminate the need for carbonates or limestone and are typically synthesised using industrial by-products like fly ash and ground granulated blast furnace slag (GGBS) [3, 4]. Numerous studies have shown that geopolymers achieve comparable or superior compressive strengths and durability relative to OPC-based materials [5]. They are particularly resistant to chemical attack and fire, and often demonstrate high early strength [6]. Geopolymer concretes have been reported to reduce CO_2 emissions by up to 80% compared to conventional OPC concrete [7]. Turner and Collins (2013) confirmed that specific geopolymer mixes emit over 80% less embodied CO_2 than OPC [7]. These attributes make geopolymers highly attractive for sustainable infrastructure applications. The geopolymerization process involves dissolving aluminosilicate materials (e.g., metakaolin, fly ash, or GGBS) in strong alkali solutions, such as NaOH and sodium silicate, initiating the rapid polymerisation into a dense Si–O–Al network [8, 9]. Depending on calcium content, the gel phases formed include calcium–(alumino)–silicate–hydrate (C-(A)-S-H) or sodium–alumino–silicate–hydrate (N-A-S-H) [9]. A standard "two-part" activator system uses NaOH and commercial sodium silicate ("waterglass"). However, manufacturing sodium silicate is highly energy-intensive, producing roughly 1.5 kg CO_2 per kg of product [10], and adds significant cost to geopolymer production [10]. These environmental and economic drawbacks limit the scalability of geopolymers in many regions. Alternative silica sources have been explored to improve sustainability. Agricultural and mineral waste materials rich in amorphous SiO_2, such as rice husk ash (RHA) and diatomaceous earth (DE), offer low-cost, sustainable substitutes for commercial sodium silicate [11]. RHA, a by-product of rice milling, contains 85–95% amorphous silica [11] and possesses high porosity and reactivity. Studies have shown that RHA can be dissolved in alkali to produce sodium silicate solutions capable of fully activating aluminosilicate precursors [12, 13]. For instance, Lima et al. (2021) demonstrated that replacing commercial waterglass with RHA-derived silicate improved the 7-day compressive strength of metakaolin geopolymers by 40%, reaching up to 6.33 MPa [12]. Similarly, DE—a sedimentary rock primarily composed of fossilised diatom silica—contains 80–90% amorphous SiO_2 [6]. Although widely used in filtration processes, much of this DE becomes waste after use [14]. Font et al. (2018) demonstrated that spent DE could partially replace commercial sodium silicate in geopolymer production, though with a slight reduction in compressive strength [14]. More recent research by Felaous et al. (2023) utilised natural diatomite activated with NaOH (8–10 M) to produce GGBS-based geopolymers, achieving 42 MPa compressive strength under ambient curing at 28 days [15]. This performance is comparable to conventional sodium silicate-based systems, with XRD and FTIR confirming the formation of typical amorphous C-(A)-S-H gels [15]. Emerging studies also suggest combining RHA and DE could enhance silica availability and optimise reaction kinetics. However, most research has focused on using these materials separately or in high-temperature-cured systems. Limited attention has been paid to ambient-cured GGBS geopolymers or exploring synergistic effects when using RHA and DE together [6, 16]. Thus, there is significant potential to develop low-carbon geopolymer formulations by replacing 5–15% of commercial sodium silicate with a combination of RHA and DE-derived activators. Such approaches could improve early and long-term mechanical performance while dramatically lowering environmental impacts [17, 18]. In conclusion, it is hypothesised that by completely substituting commercial waterglass with RHA and DE-derived silica sources, geopolymers activated using only NaOH could achieve comparable mechanical properties and durability. This innovative approach would leverage abundant waste materials to create cost-effective, low-carbon binders, accelerating the adoption of sustainable construction materials worldwide [19-22].

Chapter 2

LITERATURE REVIEW

2.1 Ordinary Portland Cement

Portland cement production is energy-consuming and a significant source of CO_2 emissions. Cement manufacturing involves heating limestone to approximately 1450 °C, using large quantities of raw materials and fossil fuels [1]. It is responsible for over 3.5 billion tonnes of cement and nearly 2.8 billion tonnes of CO_2 emissions annually—approximately 0.66 to 0.82 kilograms of CO_2 per kilogram of cement produced [1, 2]. Cement production is one of the most significant industrial contributors to CO_2 emissions and contributes 5% to over 8% of the world's emissions [1, 2]. These emissions primarily arise from the destruction of limestone and the combustion of fossil fuels to maintain high kiln temperatures [1, 2]. To reduce such emissions, firms blend cement with substances such as fly ash, slag, silica fume, and metakaolin [3]. These supplementary cementitious materials (SCMs) decrease the quantity of clinker, a dominant but CO_2-intensive ingredient, required in cement. However, manufacturing clinker continues to be a significant source of emissions [23]. Some newer, low-carbon alternatives are starting to show promise. Materials like geopolymer cements and alkali-activated binders can substantially reduce emissions [2]. Another promising option is the Limestone Calcined Clay Cement (LC^3) system, which replaces part of the clinker with a mix of calcined clay and limestone [24]. However, large-scale adoption of these newer materials faces challenges due to high costs, technical limitations, and strict regulatory requirements [25]. With global concrete demand expected to rise, cement consumption hit around 3.5 billion tonnes in 2015 and is projected to grow steadily by mid-century [2]. Rapid urbanisation and infrastructure projects drive this growth, especially in developing countries [8]. Additionally, concerns over dwindling natural resources and the rising expenses of raw material extraction further intensify the need for alternative solutions [26]. Life Cycle Assessments (LCA) demonstrate that incorporating SCMs can reduce CO_2 emissions by 15–30%, with GGBS and fly ash proving particularly effective [7]. In ultra-high-performance concrete (UHPC), partially replacing cement with SCMs cuts emissions and improves structural performance [2]. Agricultural waste ashes—like rice husk ash and palm oil fuel ash—provide additional sustainable options, especially valuable for regions with abundant agricultural by-products [11]. Innovations like accelerated carbonation and carbon capture, utilisation, and storage (CCUS) also promise to cut emissions from cement production [27]. Reusing construction and demolition waste (CDW) as raw material further supports circular economy initiatives [28]. Despite these advances, achieving large-scale industrial adoption of low-carbon technologies requires strong policy support, financial incentives, and continuous innovation [29]. A successful transition toward a more sustainable cement industry depends on close collaboration between academia, industry, and policymakers [30, 31]. In summary, while SCMs and alternative binders have helped reduce emissions, real long-term sustainability in the cement sector calls for a comprehensive strategy—combining new materials, process improvements, and policy reforms aligned with global climate goals [23, 32, 33].

2.2 Geopolymer Materials

Geopolymers are environmentally friendly binders produced by mixing industrial waste products such as fly ash and slag with alkaline liquids such as sodium hydroxide and sodium silicate [2, 3]. Introduced in the 1970s by Davidovits [3], they are now accepted as sustainable, low-carbon alternatives to ordinary cement. Despite being different in composition, they offer comparable or even superior strength to regular cement [2, 3]. In the geopolymerization process, silicon and aluminum dissolve in the alkaline solution, forming a strong, three-dimensional network of Si–O–Al bonds [8, 26]. The type of binding gel that forms depends on the calcium content. High-calcium materials create C-(A)-

S-H gel, while low-calcium systems produce N-A-S-H gel [26]. Unlike ordinary cement, geopolymers do not require heating limestone, avoiding significant CO_2 emissions [2, 3]. Some studies show they can cut CO_2 emissions by 40–80% per ton compared to regular cement [2, 3]. Because of this, they are suitable for precast building parts, fire-resistant panels, and structures requiring high durability [34]. Recently, researchers have experimented with using other waste materials such as volcanic ash [35], mine waste [36], crushed bricks [37], and demolition waste [38] to produce geopolymers. This reduces emissions further and diverts waste from landfills [39]. Environmental studies also show that geopolymers can reduce climate impact by up to 60% compared to traditional concrete [40]. Furthermore, their compatibility with 3D printing technologies opens new possibilities for greener construction practices [38]. However, there are still hurdles. The chemicals used to activate geopolymers are expensive, raw material quality can be inconsistent, and there are no widely accepted design standards [41, 42]. Researchers are also still studying the long-term performance of geopolymers under harsh environmental conditions [43, 44]. To overcome these issues, ongoing research is exploring the addition of nanomaterials [45], improving material mixes [46], and blending geopolymers with other green materials [47]. These efforts aim to make geopolymers more affordable and reliable for broader applications [48, 49]. In conclusion, geopolymers offer a powerful pathway to reduce CO_2 emissions in construction. However, to achieve widespread adoption, it is necessary to address technical challenges, lower production costs, and develop global standards for their application [50-52].

2.3 Alkali Activators in Geopolymers

The activator solution plays a crucial role in determining the performance of geopolymer binders. Typically, a combination of solid sodium hydroxide (NaOH) or potassium hydroxide (KOH) and liquid sodium silicate is used to activate aluminosilicate precursors [9]. NaOH promotes the dissolution of the precursor material, while sodium silicate supplies additional soluble silica, accelerating the geopolymerization process and enhancing early strength development [9]. However, commercial sodium silicate (commonly referred to as "waterglass") is associated with a high carbon footprint, with estimates ranging from 1.2 to 1.5 kg CO_2 per kg of Na_2SiO_3 (sodium silicate) [7]. Turner and Collins (2013) reported a global warming potential of approximately 1.5 kg CO_2 per kg of sodium silicate solution, making it one of the most carbon-intensive components of geopolymer formulations [7]. Additionally, Patro et al. (2024) highlighted that sodium silicate is expensive and one of the least sustainable materials used in geopolymer production [10]. To address these challenges, researchers are increasingly exploring “one-part” geopolymer systems, also known as just-add-water formulations, which rely on solid activators or waste-derived silicate sources [19]. These systems reduce handling difficulties and lower environmental impacts, but may sometimes compromise mechanical performance [42]. Recent advances have introduced alternative activators derived from industrial and agricultural wastes, such as rice husk ash, volcanic ash, and biomass residues, which significantly reduce embodied CO_2 emissions and energy consumption [20, 21]. Innovative solutions like pumice-derived sodium silicate have also demonstrated promising results in reducing the reliance on commercial waterglass [53]. Life Cycle Assessment (LCA) studies confirm that using waste-based activators and solid-state formulations can reduce both the environmental and economic burdens associated with geopolymer production [22, 54]. One-part systems lower CO_2 emissions, simplify on-site mixing, and improve safety by eliminating the need to handle corrosive liquid activators [45]. Despite these advancements, specific barriers remain, including the variability of waste-derived activator compositions and their influence on long-term durability and mechanical performance [46, 48]. Further research is focused on optimising activator chemistry, improving reaction kinetics, and integrating nanomaterials to enhance the performance of one-part systems [11, 13]. In summary, while selecting activators significantly influences geopolymer materials' setting time, strength, and durability, high costs and conventional sodium silicate carbon footprint remain key obstacles to broader adoption. The shift toward sustainable, cost-effective, and low-carbon alternatives is essential to realise the full potential of geopolymer technology in sustainable construction [12, 55].

2.4 Waste-Based Activators: Rice Husk Ash and Diatomaceous Earth

Rice Husk Ash (RHA) is an auspicious waste-based material, produced through the controlled combustion of rice husks, and contains about 85–95% amorphous silica [12]. This high SiO_2 content, combined with a large specific surface area, makes RHA a highly reactive pozzolan and a sustainable raw material for producing alkaline activators. Researchers have successfully dissolved RHA in NaOH to create sodium silicate solutions capable of fully activating aluminosilicates [10, 14]. For instance, Handayani et al. (2022) synthesised RHA-based silicates, achieving compressive strengths comparable to commercial sodium silicate in geopolymer mixes [13]. These results confirm that RHA is a cost-effective alternative and an environmentally friendly solution supporting circular economy goals [10]. Recent studies have further explored combining RHA with industrial wastes such as oil refining sludge and chamotte to enhance mechanical properties and reduce environmental impacts [6]. Additionally, integrating RHA into one-part geopolymer systems significantly reduces embodied CO_2 emissions and energy consumption, while maintaining satisfactory structural performance [56]. Diatomaceous Earth (DE) is a naturally occurring sedimentary material composed primarily of biogenic silica from fossilised diatoms, typically containing 80–90% SiO_2[14]. Although raw DE is often used as a filtration waste product, it exhibits pozzolanic properties when finely ground. Researchers have begun leveraging DE as a siliceous activator to replace commercial sodium silicate. Font et al. [14] demonstrated that spent filter DE mixed with NaOH could partially substitute commercial waterglass in fly ash-based geopolymers, albeit with slightly lower strength outcomes [57]. More advanced processing techniques have emerged recently. Felaous et al. [15] developed a "diatomite gel" by dissolving natural diatomite in NaOH solutions (6–10 M), successfully using it to activate ground granulated blast furnace slag (GGBS). Their optimised mix, with 8 M NaOH and 10% DE, achieved an impressive 42 MPa compressive strength under ambient curing at 28 days [14]. XRD and FTIR analyses confirmed the formation of an amorphous C-(A)-S-H gel, similar to conventional mixes. Beyond mechanical strength, DE contributes to improved thermal insulation and reduced density in geopolymer composites, making it ideal for lightweight, sustainable construction applications [14, 58]Studies also highlight that using DE as a silica source can reduce CO_2 emissions by up to 25% compared to systems relying solely on commercial waterglass [59]. While both RHA and DE have shown great promise as waste-based alkali activators, challenges remain regarding the variability of waste materials, optimisation of dissolution processes, and rheological control in practical applications [56, 60]. Continued research is essential to refine processing techniques and develop standardised formulations that ensure consistent performance [33]. In conclusion, waste-based activators derived from RHA and DE present a highly sustainable and cost-effective path for reducing carbon emissions and material costs in geopolymer production. These alternatives support global efforts toward greener construction practices while promoting effective waste management strategies [26].

2.5 Identified Research Gaps

The application of rice husk ash (RHA) and diatomaceous earth (DE) as substitute silica sources for alkali activators in ambient-cured ground granulated blast furnace slag (GGBS)-based geopolymers remains an underexplored area of research. Specifically, there is a notable lack of comprehensive investigation into the optimisation of their dosage and combined proportions to achieve a well-balanced performance in terms of mechanical strength, microstructural refinement, and long-term durability, all without the reliance on commercially available sodium silicate solutions. Although both RHA and DE have independently demonstrated potential as sustainable silica-rich activating agents in various alkali-activated systems, their exclusive use as primary or sole activators in significant quantities is relatively rare. RHA and DE's synergistic or comparative effects in geopolymer formulations, particularly under ambient curing conditions, have not been thoroughly evaluated. More importantly, no systematic studies have been conducted that treat RHA and DE as components of a single experimental system to investigate their individual and interactive impacts on key parameters such as reaction kinetics, gel phase development, and essential durability characteristics, including porosity, dimensional stability (e.g., shrinkage), and chemical resistance to aggressive environments. This research gap presents a critical challenge to advancing greener and more cost-effective geopolymer technologies. Without a deeper understanding of how RHA and DE function as alternative silica sources in the absence of commercial activators, the development of genuinely sustainable, high-performance, and economically viable geopolymer mixtures that harness the benefits of both natural mineral resources (such as DE) and agricultural waste products (such as RHA) remains limited.

2.6 Problem Formulation and Hypothesis

Based on the above, this thesis investigates geopolymer formulations using NaOH and silicate solutions derived from rice husk and diatomaceous wastes. It is hypothesised that replacing commercial waterglass with a mixture of RHA- and DE-derived sodium silicates (dissolved in NaOH) will yield geopolymers with comparable compressive strength and durability to standard mixes. The research will test mixes with varying RHA/DE ratios and NaOH molarity, flow value, 7-day and 28-day strength, density, water absorption, porosity and microstructure (via XRD, FTIR, FESEM). By utilising widely available industrial and agricultural waste materials, this approach seeks to significantly reduce the environmental footprint associated with conventional cement production, all while preserving, if not enhancing, the mechanical and durability performance of geopolymer binders for sustainable construction applications.

Chapter 3

MATERIALS AND METHODS

3.1 Raw Materials

3.1.1 Ground Granulated Blast Furnace Slag

The Ground Granulated Blast Furnace Slag (GGBS) used in this study was sourced from SUYOG ELEMENTS, India. The chemical composition was analysed using X-ray fluorescence (XRF) analysis, which revealed approximately 37.4% silicon dioxide (SiO_2), 43.7% calcium oxide (CaO), 10.8% aluminium oxide (Al_2O_3), and 6.5% magnesium oxide (MgO). Due to its high calcium content and inherent pozzolanic and latent hydraulic properties, GGBS is well-suited for ambient-cured geopolymer systems [15].

3.1.2 Rice Husk Ash

Rice Husk Ash (RHA) was obtained from Herenba Instruments and Engineers, India. Before use, the ash was oven-dried at 100 ± 5 °C for 24 hours to remove residual moisture. Thermogravimetric analysis showed a very low loss on ignition (~1.4%), indicating nearly complete combustion of the husks. XRF analysis confirmed that RHA contains approximately 80-90% silica, primarily in the amorphous form, making it a highly reactive and effective source of silica for geopolymer binder synthesis [12].

3.1.3 Diatomaceous Earth

The Diatomaceous Earth (DE) in powder form was obtained from the commercial market. The material was similarly dried at 100 ± 5 °C for 24 hours. XRF analysis showed a silica content of approximately 82%, along with 2–3% aluminium oxide and 0–2% calcium oxide [14]. RHA and DE were used as alternative silica sources to prepare the sodium silicate-type activator solution.

3.1.4 Alkali Activators

The alkali activator solution was prepared using analytical-grade sodium hydroxide (NaOH) pellets with a purity greater than 98%. A 10 M NaOH solution was made by dissolving 380.8 grams of NaOH in 952.4 millilitres of distilled water. After cooling to room temperature, RHA or DE was incorporated into the solution at different percentages of 0%, 5%, 10%, and 15% by weight of GGBS. Each mixture was agitated for 25 minutes to ensure complete dispersion and uniformity of the silica-rich solution.

3.2 Experimental Details

3.2.1 Preparation of Activator Solutions

Table 1 provides the nomenclature and detailed mix proportions of geopolymer formulations incorporating RHA and DE at varying percentages

Sample	**GGBS (g)**	**NaOH Molarity (M)**	**Water (ml)**	**NaOH (g)**	**DE/RH (%)**	**L/S Ratio**	**Additional Water (ml)**
NH	2400	10	952.4	380.8	0	0.55	0
DE5/ RH5	2400	10	952.4	380.8	5	0.55	100
DE10/ RH10	2400	10	952.4	380.8	10	0.55	210
DE15/ RH15	2400	10	952.4	380.8	15	0.55	315

Table 1-Nomenclature and mix design of geopolymers.

Note: Additional water was added to maintain consistent workability (190 ± 10 mm, measured via flow table test).

As shown in the following Figure 3.1, the step-by-step preparation of the activator solution involves the controlled dissolution of sodium hydroxide, followed by the dispersion of RHA or DE to form a silica-rich alkali medium.

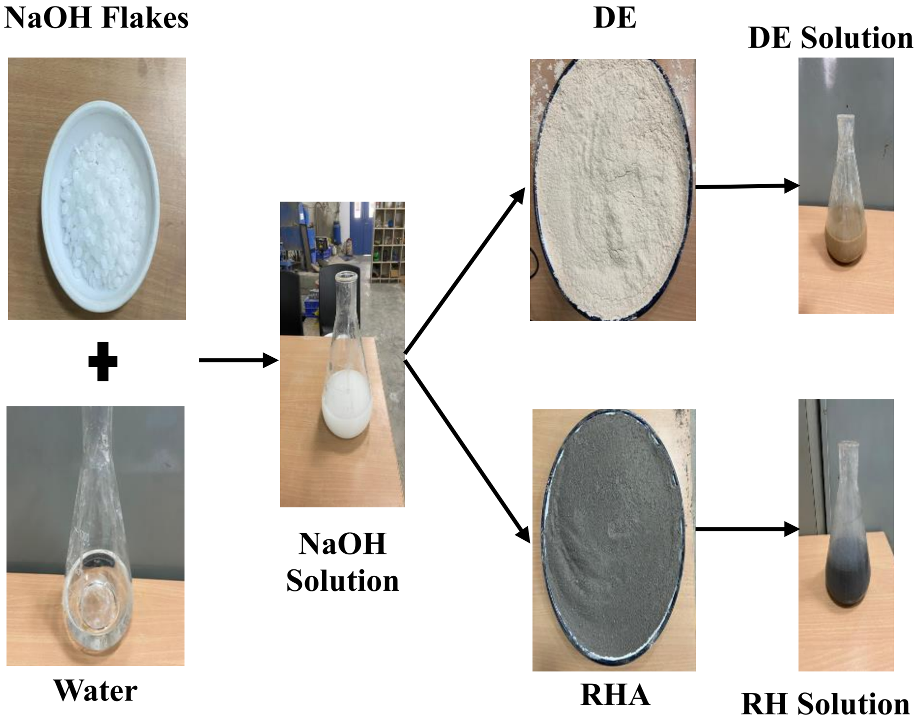

Figure 3.1: Preparation of activator solution.

The activator solutions were prepared according to the mix proportions shown in Table 1. Once the sodium hydroxide (NaOH) solution was cooled to room temperature, predetermined amounts of rice husk ash (RHA) or diatomaceous earth (DE) were added. The mixtures were stirred continuously for 25 minutes to ensure complete dispersion and uniform solution formation.

3.2.2 Geopolymer Synthesis

Figure 3.2 illustrates the casting process of geopolymer mortar cubes, where the activator-blended GGBS paste is thoroughly mixed, tested for flow, and poured into cube moulds to prepare samples for testing.

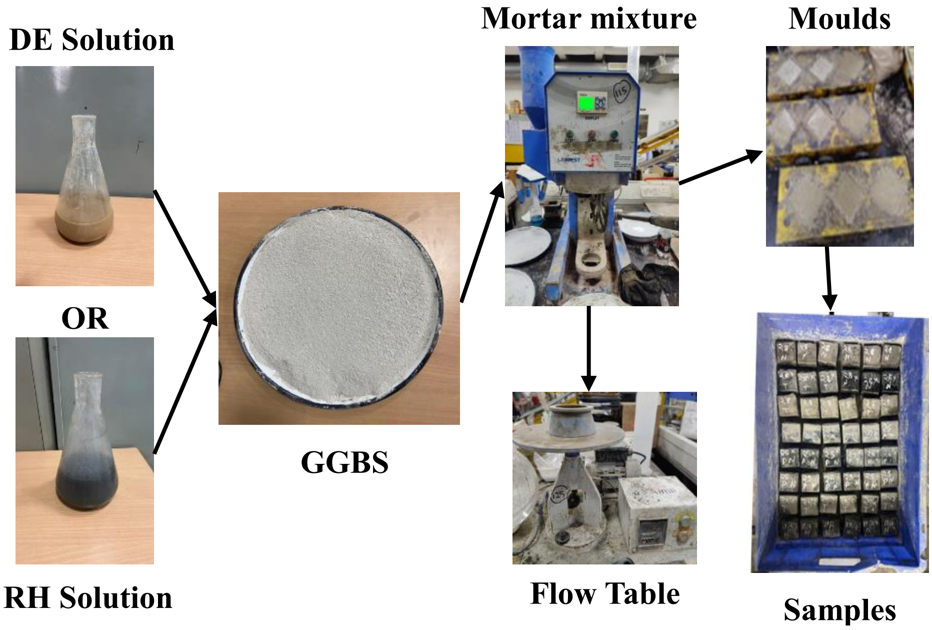

Figure 3.2: Casting of geopolymer mortar.

Geopolymer binder samples were synthesised. A fixed mass of 2400 grams of ground granulated blast furnace slag (GGBS) was combined with the corresponding activator solution, as described in Table 1. The materials were mixed thoroughly for 5 minutes to produce a homogeneous paste. The workability of fresh geopolymer mortar was evaluated using a standard flow table as specified in ASTM C230 61]. The paste was then cast into 50 mm cube moulds in two layers, each compacted using a vibrating table to eliminate air voids and ensure proper consolidation. All samples were cured under ambient conditions.

3.2.3 Curing Regime

After 24 hours, the samples were removed from the mould and cured at ambient temperature (25°C to 30°C). No external heat treatment was applied. Compressive strength tests were performed at 7 and 28 days following the Indian Standard IS: 516 (1959) [62].

3.3 Characterisation Methods

3.3.1 X-ray diffraction Analysis

Figure 3.3 shows the sample preparation and experimental setup used for X-ray diffraction (XRD) analysis to characterise phase composition in raw materials and geopolymer specimens.

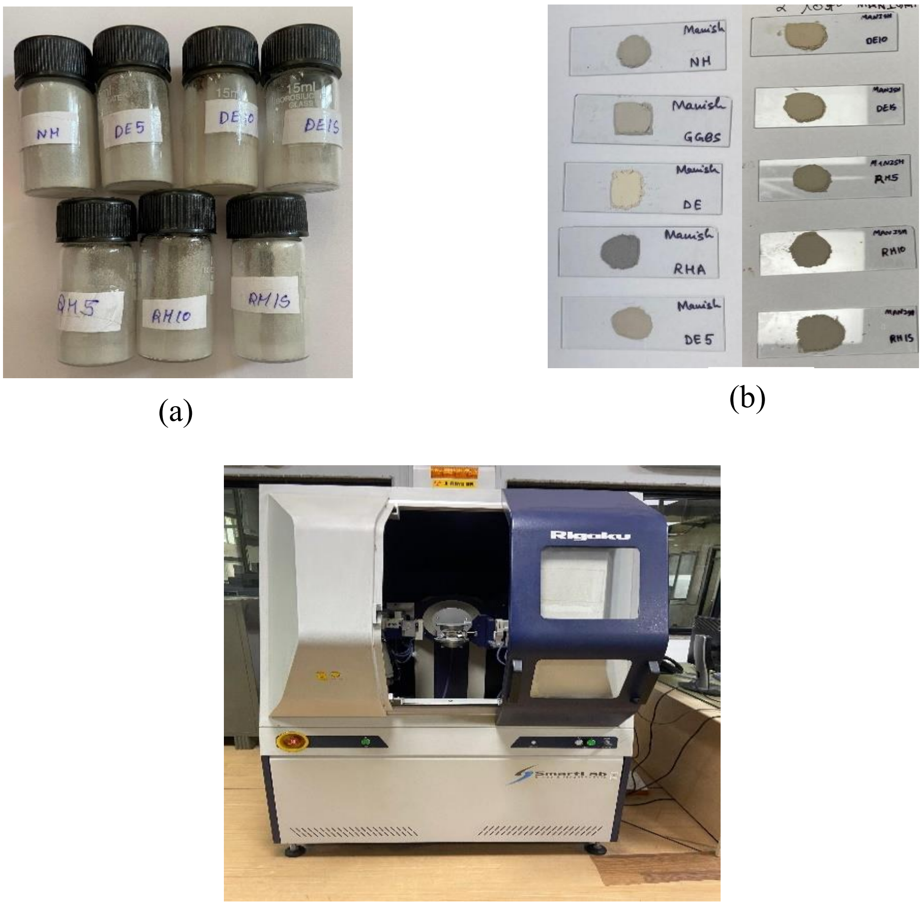

(a) (b)

(c)

Figure 3.3: (a) Powder sample, (b) Sample spotted on glass plate, (c) X-ray Diffractometer.

XRD analysis uses a Rigaku SmartLab X-ray Diffractometer equipped with a 2.2 kW Cu Kα radiation source to identify crystalline and amorphous phases in the raw materials and geopolymer matrices. The instrument operated in continuous scan mode with a step size of 0.04°

2θ over a range of 5°–90°. Powdered samples (<75 μm), prepared by grinding with an agate mortar and pestle, were directly used for analysis.

3.3.2 Fourier-Transform Infrared Spectroscopy

Fourier-Transform Infrared Spectroscopy (FTIR) analysis uses a Bruker Alpha II FTIR spectrometer equipped with a Diamond ATR accessory to investigate the chemical bonding and functional groups in the raw materials and geopolymer matrices. Spectra were displayed within the wavenumber range of 400 to 4000 cm^{-1}. Figure 3.4 shows a powder sample and the spectrometer used for functional group identification.

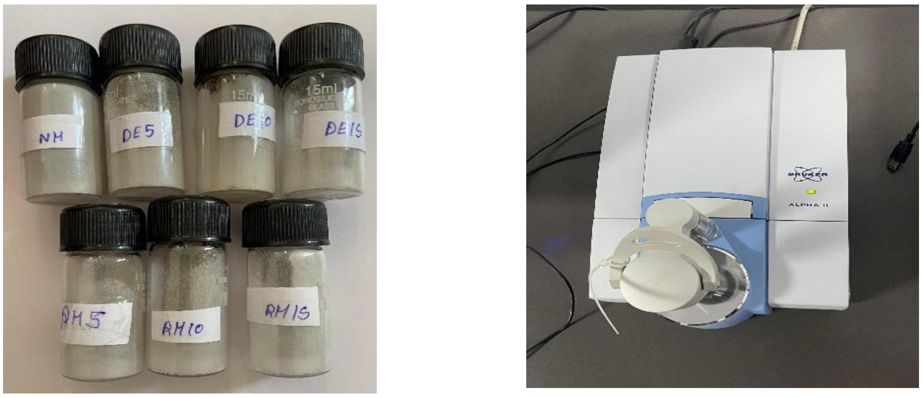

(a) (b)

Figure 3.4: (a) Powder sample, (b) Bruker Alpha II FTIR spectrometer.

3.3.3 Field Emission Scanning Electron Microscopy with Energy Dispersive Spectroscopy

Microstructural imaging and elemental analysis were carried out utilising a ZEISS GeminiSEM 360 Field Emission Scanning Electron Microscope (FESEM). The imaging was performed under high vacuum conditions with an accelerating voltage ranging from 5 to 20 kV. To improve conductivity, samples were coated with gold using a Quorum Q150R ES Sputter Coater. The drop-casting method was used for raw materials (GGBS, DE, RHA) by dispersing powders in acetone and dropping them onto a glass plate. Geopolymer samples (NH, DE5, DE10, DE15, RH5, RH10, RH15) were cut, polished with abrasive papers (600–2000 grit), and then gold-coated before analysis.

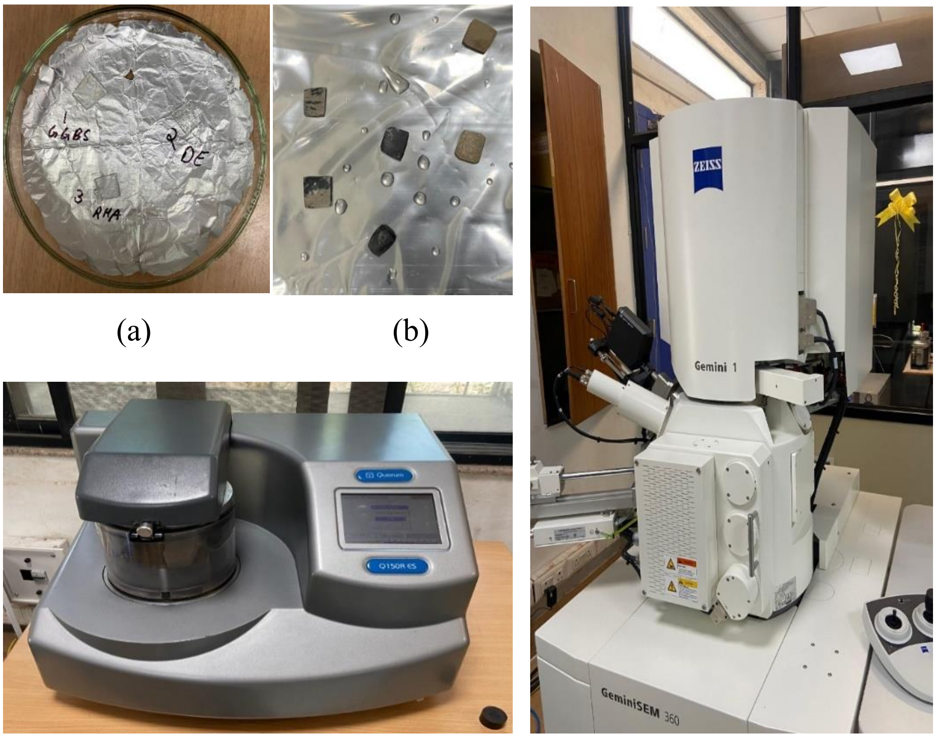

(a) (b)

(c) (d)

Figure 3.5: (a) Drop-Casted samples, (b) Polished geopolymer sample, (c) Quorum Q150R ES Sputter Coater, (d) ZEISS GeminiSEM 360 FESEM instrument.

Figure 3.5 shows the prepared samples and equipment used for FESEM–EDS analysis. FESEM images were captured at 2000, 5000, and 10,000 magnifications to examine morphological features in detail. EDS was performed to identify the elemental composition of selected regions and to support microstructure composition correlation.

3.3.4 Compressive Strength Testing

Figure 3.6 presents the compressive strength testing process, showing cube samples before and after testing and the equipment used for controlled load application.

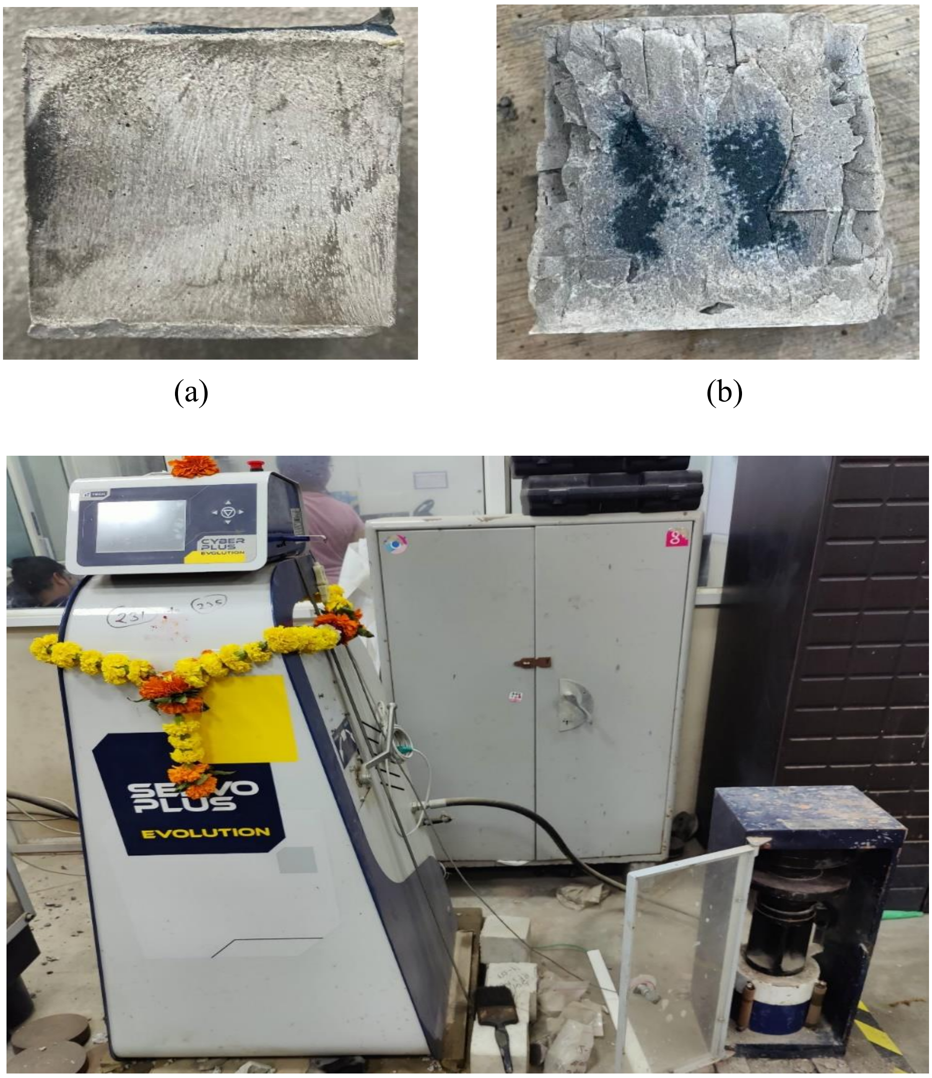

(a) (b)

(c)

Figure 3.6: (a) Cube sample before testing, (b) Cube sample after testing, (c) Compression Testing Machine.

Compressive strength was evaluated on 50 mm cube specimens using a Servo Plus Evolution Compression Testing Machine equipped with a Cyber Plus Interface. The loading rate was maintained at 0.23 kN/s. While this rate is lower than the ASTM C109 recommended range [63], it was adopted to avoid brittle failure and to ensure accurate load control during compressive strength evaluation of ambient-cured geopolymer paste specimens.

3.3.5 Physical and Durability Properties (Bulk Density, Porosity, and Water Absorption)

Bulk density, porosity, and water absorption tests were performed to assess the compactness and permeability of the hardened geopolymer matrix, following ASTM C642-21 guidelines [64]. For porosity and absorption measurements, specimens were fully saturated under vacuum. The bulk density was calculated by dividing the mass of the dry specimen by its volume; water absorption was evaluated by measuring the mass increase after immersion, and porosity was derived by taking the difference between the saturated and dry masses relative to the volume of the specimen.

Chapter 4

RESULTS

4.1 Characterisation of Raw Material

Figure 4.1 presents the X-ray diffraction (XRD) patterns of GGBS, DE, and RHA, illustrating their degree of crystallinity and amorphous content. These patterns provide insight into the phase composition of each material and their potential reactivity under alkali activation. A broad amorphous hump indicates high reactivity, while sharp peaks correspond to crystalline phases that may remain unreacted. The identification of calcite, quartz, or cristobalite helps in correlating the mineral structure with mechanical performance.

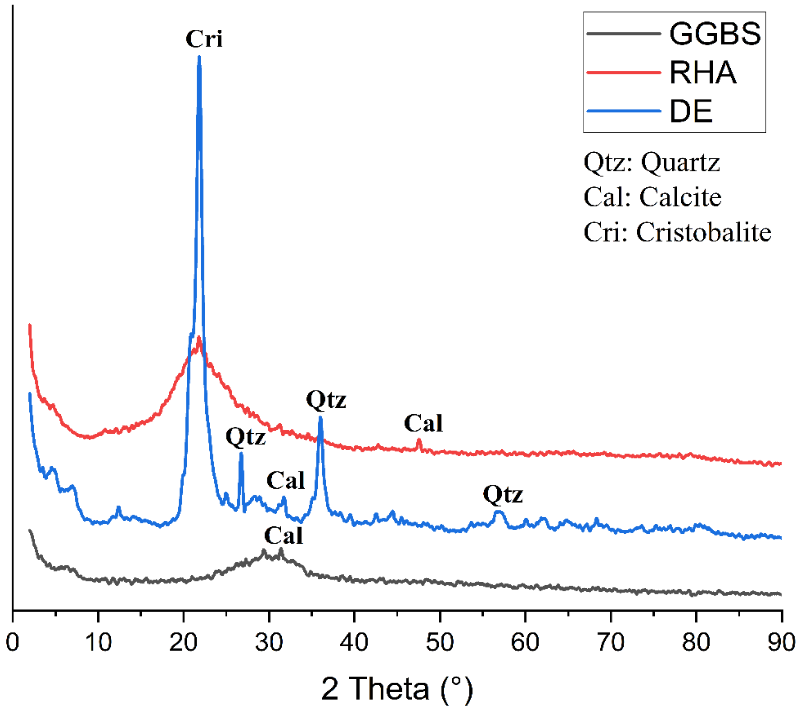

Figure 4.1: XRD pattern of GGBS, DE, RHA.

The functional group characteristics of GGBS, DE, and RHA were examined using FTIR spectroscopy, as shown in Figure 4.2. The absorption bands help identify the key bonding environments and confirm the presence of reactive silicate and aluminate structures in the raw materials. FTIR serves as a useful tool to distinguish between amorphous and crystalline silica phases in these systems. Specific vibrational modes such as Si–O–Si and Si–O–Al provide information on the polymerisation potential of each material.

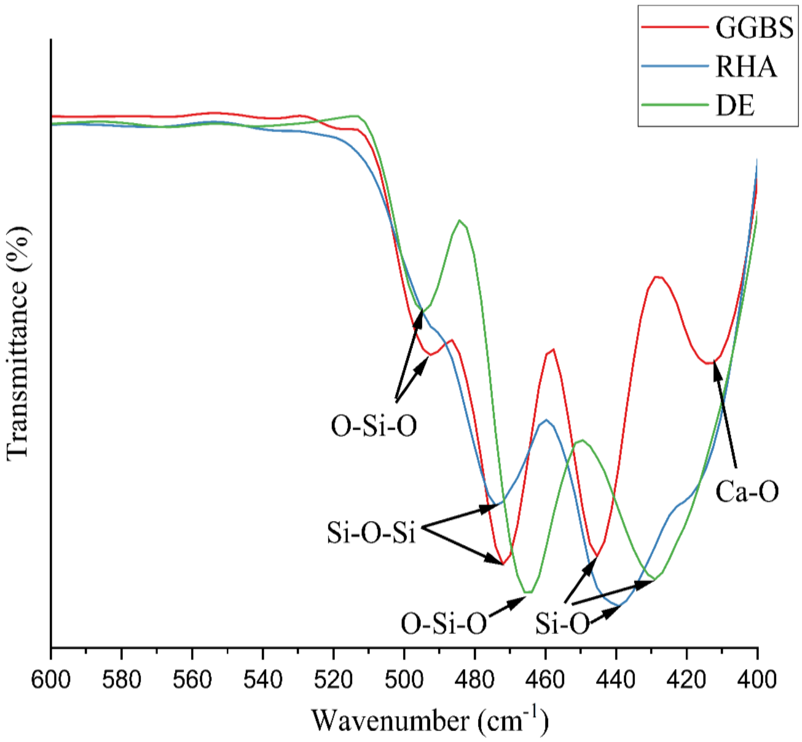

Figure 4.2: FTIR spectrum of GGBS, DE, RHA.

Figure 4.3 displays the FESEM micrographs and corresponding EDS spectra for DE and RHA. These analyses reveal the surface morphology and elemental composition of the materials, which are crucial for understanding their reactivity and suitability as silica sources in geopolymer synthesis. Morphological features such as porosity and particle shape influence dissolution behaviour during activation. The

EDS results further validate the silica-rich nature of both materials and highlight minor elemental impurities relevant to geopolymerisation.

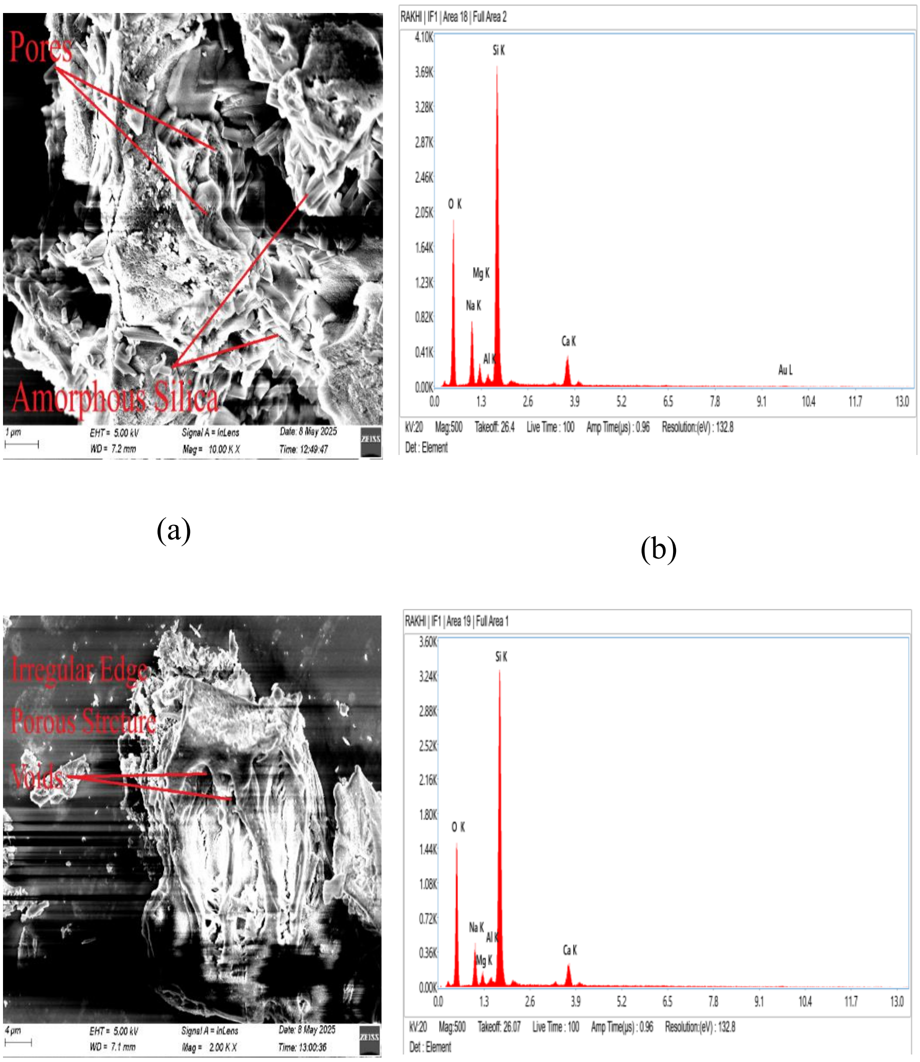

(a) (b)

(c) (d)

Figure 4.3: (a) FESEM image of DE, (b) EDS spectrum of DE, (c) FESEM image of RHA, (d) EDS spectrum of RHA.

4.1.1 Ground Granulated Blast Furnace Slag

XRD and FTIR analyses were performed to explore the phase composition, crystallinity, and functional groups present in Ground Granulated Blast Furnace Slag (GGBS). The XRD pattern, as shown in Figure 4.1, exhibited a broad amorphous hump between 22° and 38° 2θ, confirming the predominantly glassy and amorphous structure of GGBS, which is favourable for geopolymerization by promoting the dissolution of reactive species and facilitating C-A-S-H gel formation. Minor crystalline peaks were noticed at approximately 29° 2θ corresponding to Calcite, as per the JCPDS standard, and a small peak at around 31° 2θ attributed to either a secondary reflection of Calcite or possible residual calcium silicate phases. No notable quartz peaks were detected, indicating minimal crystalline silica content and confirming the high reactivity potential of GGBS. The FTIR analysis shown in Figure 4.2 further confirmed these results, highlighting significant absorption bands at 492.5 cm^{-1} associated with O–Si–O bending vibrations, 472 cm^{-1} linked to Si–O–Si symmetric stretching vibrations, 445 cm^{-1} connected to the bending of Si–O in silicate tetrahedra, and 414 cm^{-1} related to the stretching vibrations of Ca–O. These vibrational bands confirm the presence of reactive silicate species and available calcium ions essential for geopolymerization reactions.

4.1.2 Diatomaceous Earth

XRD, FTIR, FESEM and EDS were utilised to evaluate Diatomaceous Earth's mineralogical, structural, and chemical properties (DE). The XRD pattern, shown in Figure 4.1, reveals a crystalline-rich profile with several sharp and intense peaks. A prominent peak at approximately 21° 2θ indicates the presence of Cristobalite, a high-temperature polymorph of silica typically found in diatomaceous earth. Well-defined peaks at around 26.6°, 36°, and 50° 2θ confirm the presence of Quartz, while additional reflections at 29° and 31° 2θ are attributed to Calcite and possibly residual calcium silicate phases, indicating minor carbonate impurities. The dominance of Cristobalite and Quartz suggests a limited availability of reactive amorphous silica, which may reduce the material's reactivity unless thermally or mechanically activated. FTIR analysis, presented in Figure 4.2, supports these findings, exhibiting absorption bands at 494 cm^{-1} assigned to O–Si–O bending vibrations from silicate frameworks, 465 cm^{-1} corresponding to Si–O–Si symmetric stretching, and 428 cm^{-1} related to Si–O bending vibrations in less polymerised or disordered silica networks. These bands indicate the presence of silica, though it exists in a rigid or partially crystalline structure. The FESEM image in Figure 4.3(a) shows a highly porous structure DE, with a well-defined pore structure. However, the persistence of intact biological shapes implies incomplete structural degradation, which corresponds with the crystalline peaks seen in XRD. The EDS spectrum depicted in Figure 4.3(b) verifies a composition abundant in silica, characterised by elevated levels of silicon and oxygen. Some trace elements like sodium, magnesium, aluminium, and calcium were identified in small concentrations. The limited calcium content aligns with FTIR observations showing no Ca–O related peaks, indicating that DE acts primarily as a silica source with minimal contribution to calcium-based gel formation in geopolymer systems.

4.1.2 Rice Husk Ash

XRD, FTIR, FESEM and EDS analyses were carried out to assess the structural and chemical properties of Rice Husk Ash (RHA). The XRD pattern shown in Figure 4.1 exhibits a broad amorphous hump starting around 17° 2θ and extending to 26° 2θ, characteristic of amorphous silica. No distinct peak is observed at approximately 21.88° 2θ, confirming the absence of crystalline phases such as Cristobalite, and the typical Quartz peak at around 26.6° 2θ is also absent, indicating that RHA is predominantly composed of amorphous silica. This highly disordered non-crystalline structure makes RHA exceptionally reactive, making it a highly effective silica source for geopolymer applications. FTIR analysis, presented in Figure 4.2, further supports these observations, showing strong absorption bands at 474 cm^{-1}

corresponding to O–Si–O bending vibrations, confirming the dominance of amorphous silica phases, and 439 cm^{-1} assigned to Si–O bending vibrations associated with well-developed silicate tetrahedra. The sharp and intense nature of these peaks reflects the high chemical reactivity of RHA and its suitability for rapid geopolymerization. The FESEM image in Figure 4.3(c) shows highly irregular, porous particles with rough surface textures, contributing to a large surface area that enhances silica dissolution in alkaline environments. No biological or unprocessed structures are visible, indicating that the ash was properly calcined and processed. The EDS spectrum in Figure 4.3(d) confirms a dominant silicon peak, indicating high amorphous silica content, and a high oxygen concentration due to silicate bonds. Trace amounts of sodium, magnesium, aluminium, and calcium were also detected, which may contribute marginally to the formation of geopolymer gels. These results confirm that RHA is chemically pure and structurally well-suited for geopolymer synthesis as a reactive silica source.

4.2 Characterisation of Synthesised Geopolymers

4.2.1 Compressive Strength

Figure 4.4 illustrates compressive strength development across different geopolymer mixes incorporating varying amounts of DE and RHA.

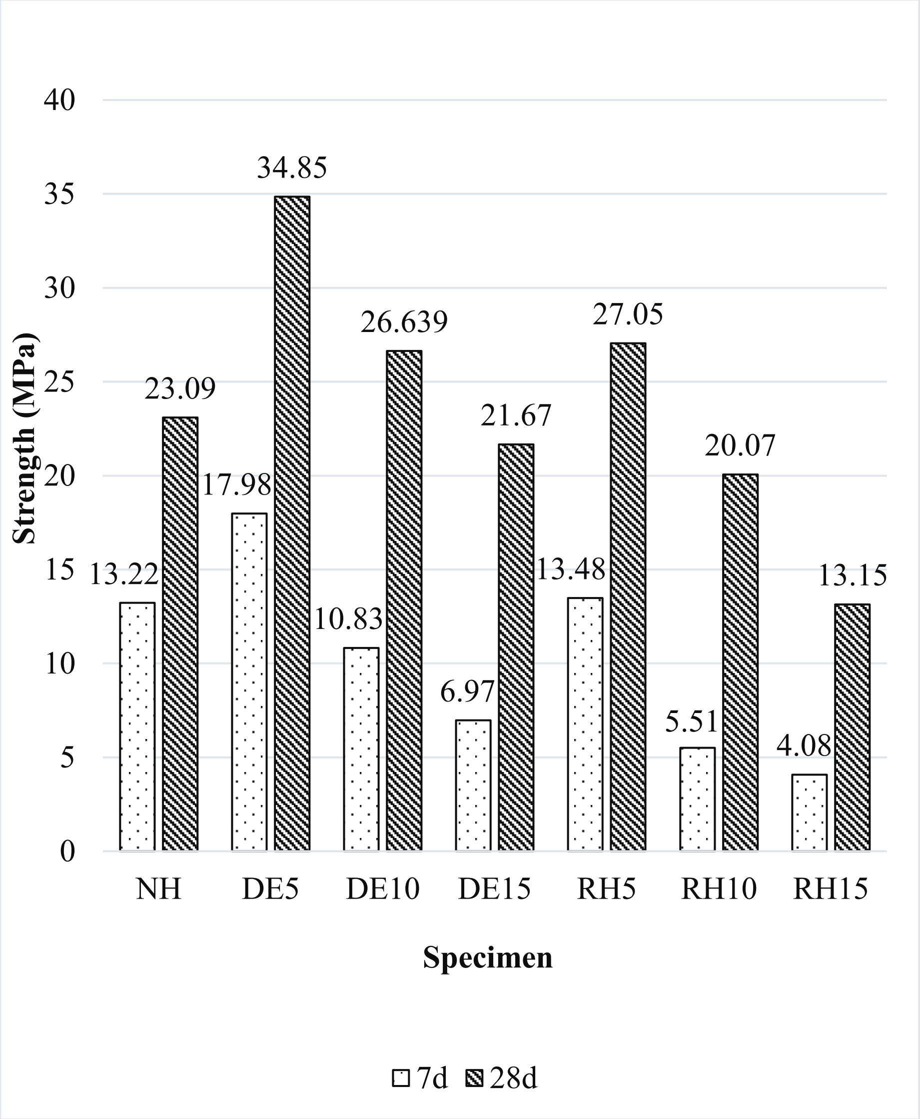

Figure 4.4: Compressive strength**.**

The compressive strength evaluation of geopolymer samples over curing periods of 7 and 28 days, as illustrated in Figure 4.4, reveals a distinct progression in mechanical performance associated with continued geopolymerization reactions and gel network densification. The reference sample NH achieved compressive strengths of 13.22 MPa at 7 days and 23.09 MPa at 28 days, indicating moderate strength development without additional reactive silica sources. Samples incorporating diatomaceous earth (DE) exhibited enhanced early and long-term strength, with DE5 achieving the highest values of 17.98 MPa at 7 days and 34.85 MPa at 28 days, reflecting efficient formation of a compact aluminosilicate gel matrix. However, increasing the DE content to 10% and 15% resulted in a decline in strength, with DE10 recording 10.83 MPa and 26.64 MPa, and DE15 reducing further to 6.97 MPa and 21.67 MPa at 7 and 28 days, respectively, suggesting that higher DE content may lead to excess unreacted silica and microstructural defects. Similarly, the RHA-modified samples followed the same trend, where RH5 achieved compressive strengths of 13.48 MPa at 7 days and 27.05 MPa at 28 days, indicative of effective reaction of amorphous silica. With higher RHA content, compressive strength decreased significantly; RH10 recorded 5.51 MPa at 7 days and 20.07 MPa at 28 days, while RH15 showed the lowest strengths at 4.08 MPa and 13.15 MPa, respectively. This progressive variation in compressive strength highlights the influence of silica source and content on the formation and quality of the geopolymer gel matrix over time.

4.2.2 Density, Porosity, and Water Absorption

Figure 4.5 presents the measured bulk density, water absorption, and porosity values, highlighting the impact of increasing waste-based silica content.

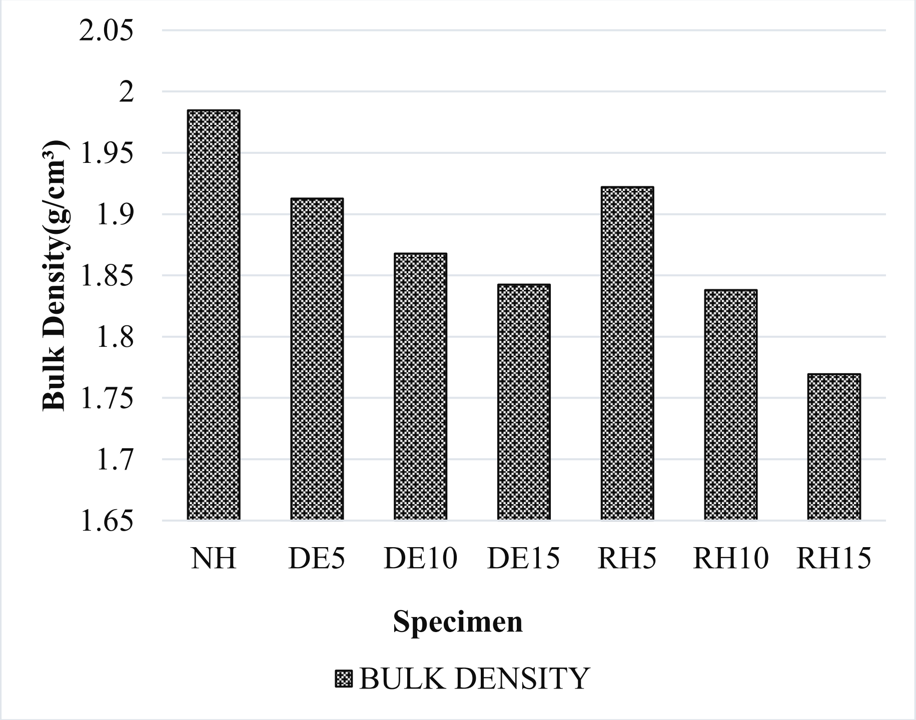

Figure 4.5(a): Bulk density.

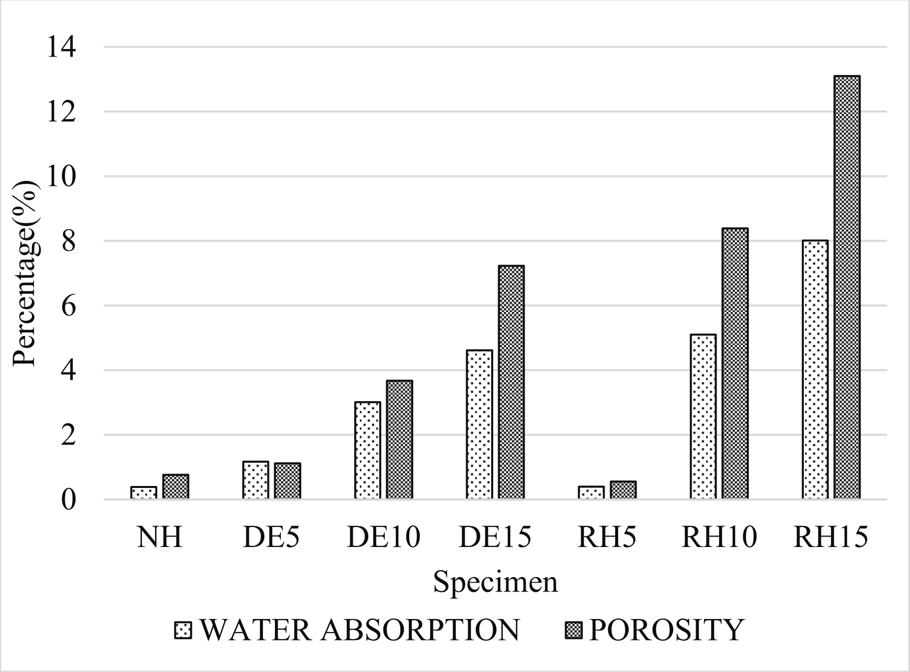

Figure 4.5(b): Water absorption and porosity.

The results presented in Figure 4.5(a) and Figure 4.5(b) demonstrate that the bulk density of geopolymer samples systematically decreases with the incorporation of diatomaceous earth (DE) and rice husk ash (RHA). The highest bulk density is recorded for the control sample NH at 1.98 g/cm³, followed by DE5 and RH5 at 1.91 g/cm³ and 1.92 g/cm³, respectively. As the addition levels of DE and RHA increase to 10% and 15%, the density further declines, reaching minimum values of 1.84 g/cm³ for DE15 and 1.77 g/cm³ for RH15, indicating the influence of higher addition content in introducing increased porosity and reducing matrix compactness. Correspondingly, water absorption and porosity exhibit a clear increasing trend with higher addition levels. Water absorption rises from 0.38% for NH to 4.60% for DE15 and significantly higher to 8.00% for RH15, reflecting the higher inherent porosity and capillary pore volume in samples containing higher RHA content. Similarly, porosity increases from 0.76% in NH to 7.23% in DE15.It attains a peak of 13.10% in RH15, demonstrating the substantial influence of RHA's porous and reactive characteristics in enhancing the interconnected voids within the matrix. This behaviour supports the notion that a greater inclusion of DE and RHA decreases material density, encourages capillary pore development, and increases porosity and water absorption.

4.2.3 XRD Analysis

i) XRD of Geopolymer Samples with DE

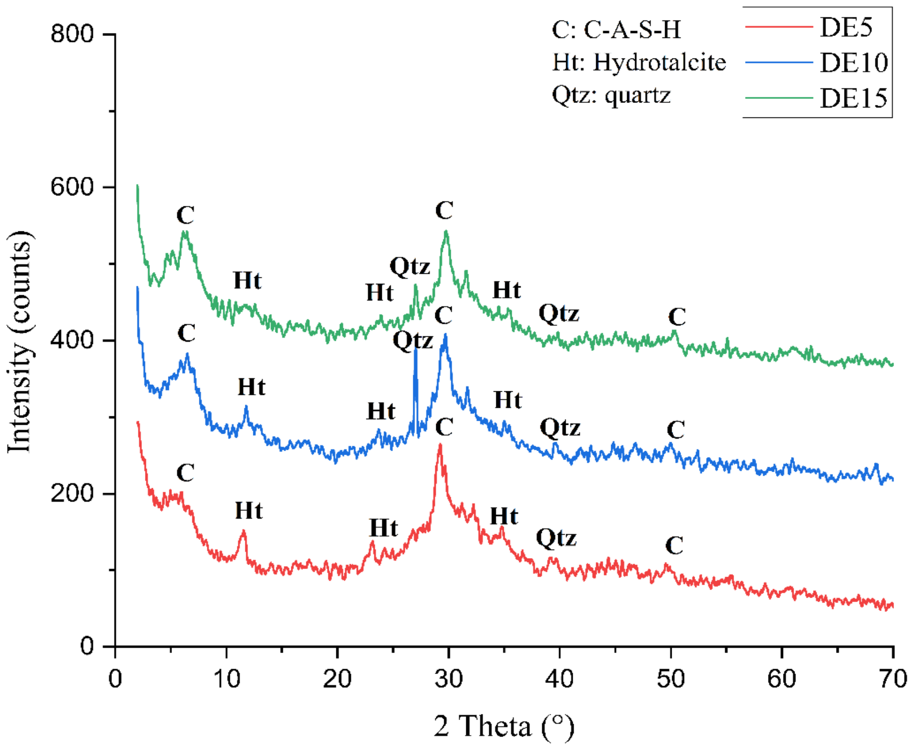

Figure 4.6: XRD patterns of geopolymer samples with DE.

The X-ray diffraction patterns in Figure 4.6 illustrate the mineralogical composition of geopolymer samples with varying diatomaceous earth (DE) content, labelled as DE5, DE10, and DE15, corresponding to 5%, 10%, and 15% DE addition levels, respectively. The patterns show an apparent reduction or disappearance of crystalline peaks associated with quartz and calcite, indicating their consumption during the geopolymerization process. New diffraction peaks appear at approximately 7.12°, 29.21°, and 49.44° 2θ, corresponding to the formation of the calcium-alumino-silicate-hydrate (C-A-S-H) gel phase. Additional peaks at 11.44°, 23.2°, and 34.82° 2θ indicate the formation of Hydrotalcite, a magnesium-aluminium layered double hydroxide with the chemical formula $(Mg_4Al_2)(OH)_{12}(CO_3)(H_2O)_3$. A prominent peak is also observed at approximately 31.36° 2θ, which is associated with semi-crystalline phases related to C-A-S-H gel development or possible calcium silicate hydrate structures formed during the reaction. A distinct peak near 26.6° to 27° 2θ remains visible in DE10 and DE15 samples, indicating the presence of residual crystalline quartz. The amorphous phase halo between 25° and 35° 2θ becomes progressively more pronounced with increasing DE content, and its intensity is notably higher in DE10 and DE15 compared to DE5, indicating increased gel formation and development of the disordered aluminosilicate network with higher DE incorporation.

ii) XRD of Geopolymer Samples with RHA.

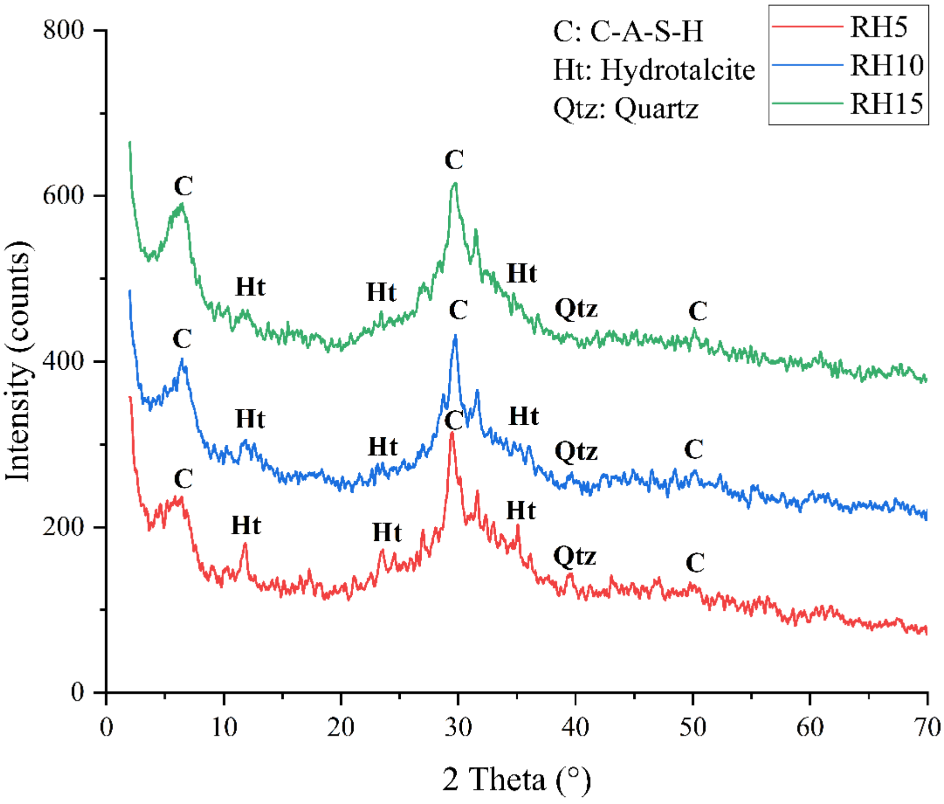

Figure 4.7: XRD patterns of geopolymer samples with RHA.

The X-ray diffraction patterns shown in Figure 4.7 illustrate the mineralogical composition of geopolymer samples prepared with varying amounts of rice husk ash (RHA), labelled as RH5, RH10, and RH15, corresponding to 5%, 10%, and 15% RHA addition levels, respectively. The patterns demonstrate significant changes in phase composition, where the intensity of crystalline peaks associated with quartz and calcite progressively decreases, indicating their partial consumption during the geopolymerization process. New diffraction peaks appear at approximately 7.12°, 29.21°, and 49.44° 2θ, corresponding to the formation of the calcium-alumino-silicate-hydrate **(**C-A-S-H**)** gel phase, which is primarily responsible for structural binding in the geopolymer matrix. Additionally, the appearance of peaks at 11.44°, 23.2°, and 34.82° 2θ confirms the formation of Hydrotalcite, a magnesium-aluminium layered double hydroxide with the chemical formula $(Mg_4Al_2)(OH)_{12}(CO_3)(H_2O)_3$, contributing to improved chemical stability and microstructural refinement. A prominent peak is also observed at approximately 31.36° 2θ, which is associated with semi-crystalline phases related to C-A-S-H gel development or possible calcium silicate hydrate structures formed during the reaction, and the intensity of this peak increases with increasing RHA content, further indicating progressive gel formation. No peak is observed at or near 26.6° 2θ in any of the RHA samples, confirming the absence of residual crystalline quartz. The amorphous phase halo, centred between 25° and 35° 2θ, becomes increasingly intense with higher RHA content, particularly in RH10 and RH15, reflecting a greater degree of geopolymer gel formation and the development of a disordered aluminosilicate network with increased RHA incorporation.

iii) XRD of Geopolymer Samples NH, DE5, and RH5

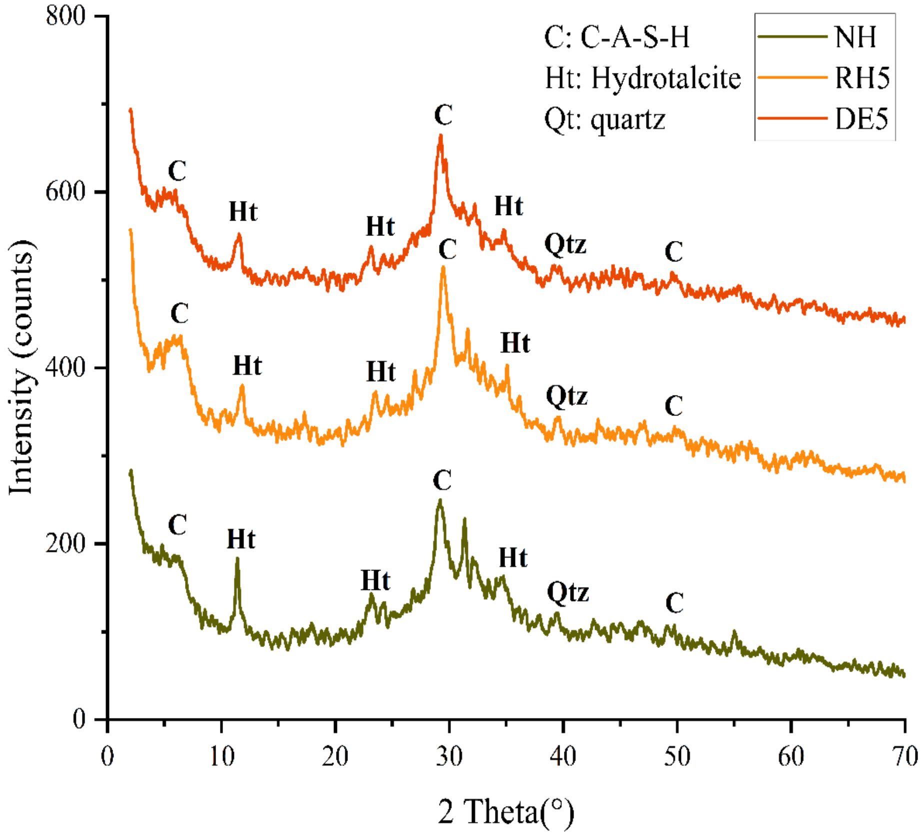

Figure 4.8: XRD patterns of geopolymer samples NH, DE5, and RH5.

The X-ray diffraction patterns shown in Figure 4.8 represent the mineralogical composition of geopolymer samples prepared with different precursor materials: NH (without additive), RH5 (5% rice husk ash), and DE5 (5% diatomaceous earth). The patterns exhibit significant phase transformations during geopolymerization, as indicated by the reduction or disappearance of initial crystalline peaks and the appearance of new reaction products. Distinct diffraction peaks are observed at approximately 7.12°, 29.21°, and 49.44° 2θ, corresponding to the formation of the calcium-alumino-silicate-hydrate (C-A-S-H) gel phase, which plays a vital role in matrix cohesion and strength development. Additional peaks at 11.44°, 23.2°, and 34.82° 2θ confirm the formation of Hydrotalcite, a magnesium-aluminium layered double hydroxide with the chemical formula $(Mg_4Al_2)(OH)_{12}(CO_3)(H_2O)_3$, which contributes to improved chemical stability and microstructural refinement. A prominent peak is also observed at approximately 31.36° 2θ, which is associated with semi-crystalline phases related to C-A-S-H gel development or possible calcium silicate hydrate structures formed during the reaction. Notably, the characteristic Quartz peak typically expected near 26.6° to 27° 2θ is absent in all samples, indicating adequate consumption of crystalline silica throughout the geopolymerization process. The broad amorphous halo centred between 25° and 35° 2θ becomes increasingly pronounced in RH5 and DE5 compared to the NH sample, reflecting enhanced gel formation and greater development of the amorphous aluminosilicate network due to the incorporation of rice husk ash and diatomaceous earth.

4.2.4 FTIR Analysis

i) FTIR of Geopolymer Samples with DE

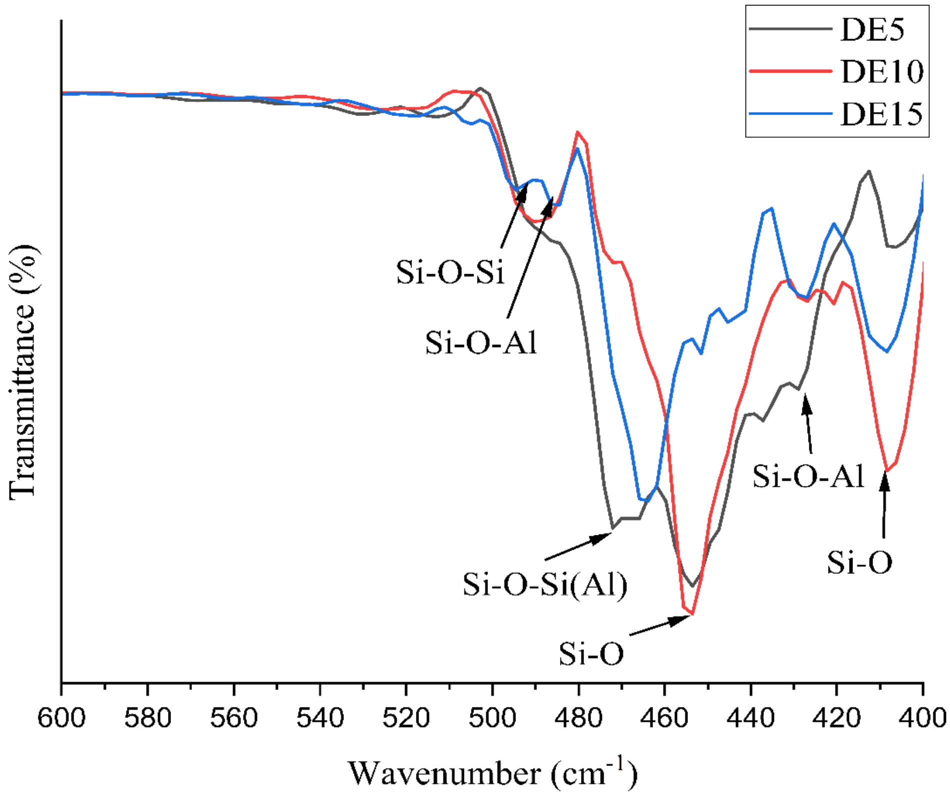

Figure 4.9: FTIR spectra of geopolymer samples with DE.

The FTIR spectra depicted in Figure 4.9 provide a detailed assessment of geopolymer matrices' polymerisation behaviour and structural evolution, incorporating varying levels of diatomaceous earth (DE), specifically DE5, DE10, and DE15. In the DE5 sample, sharp, well-defined peaks at 472 cm^{-1} and 467 cm^{-1} correspond to Si–O–Si and Si–O–Al asymmetric stretching vibrations, forming a highly polymerised and stable silicate and aluminosilicate gel network. The presence of additional peaks at 453 cm^{-1} and 437 cm^{-1}, which are associated with Si–O bending and Si–O–Al bond vibrations, respectively, further supports the successful integration of aluminium into the silicate framework, leading to an increased cross-linking density. The broad and weak peaks observed at 428 cm^{-1} and 406 cm^{-1} indicate the existence of minor unreacted silicate species or localised structural imperfections. With increasing DE content in DE10, a broader peak at 490 cm^{-1} emerges, indicating a shift toward increased structural disorder. However, the continued appearance of a sharp peak at 453 cm^{-1} reflects sustained development of the aluminosilicate network. Moderate peaks at 426 cm^{-1} and 408 cm^{-1} highlight the persistence of amorphous phases and incomplete reaction of reactive silica. In DE15, the spectrum exhibits a weak and broadened peak at 494 cm^{-1}, characteristic of strained Si–O–Si and Si–O–Al bonding environments, along with a sharp but low-intensity peak at 484 cm^{-1}, indicating the residual presence of unreacted or crystalline silica. The progressive broadening and attenuation of peaks at 465 cm^{-1}, 451 cm^{-1}, 426 cm^{-1}, and 408 cm^{-1} reflect increased network disorder and incomplete geopolymerization at higher DE contents, suggesting that although higher silica availability is introduced, it does not fully participate in the gel network formation, potentially compromising the long-term durability and structural integrity of the resulting geopolymer composites.

ii) FTIR of Geopolymer Samples with RHA

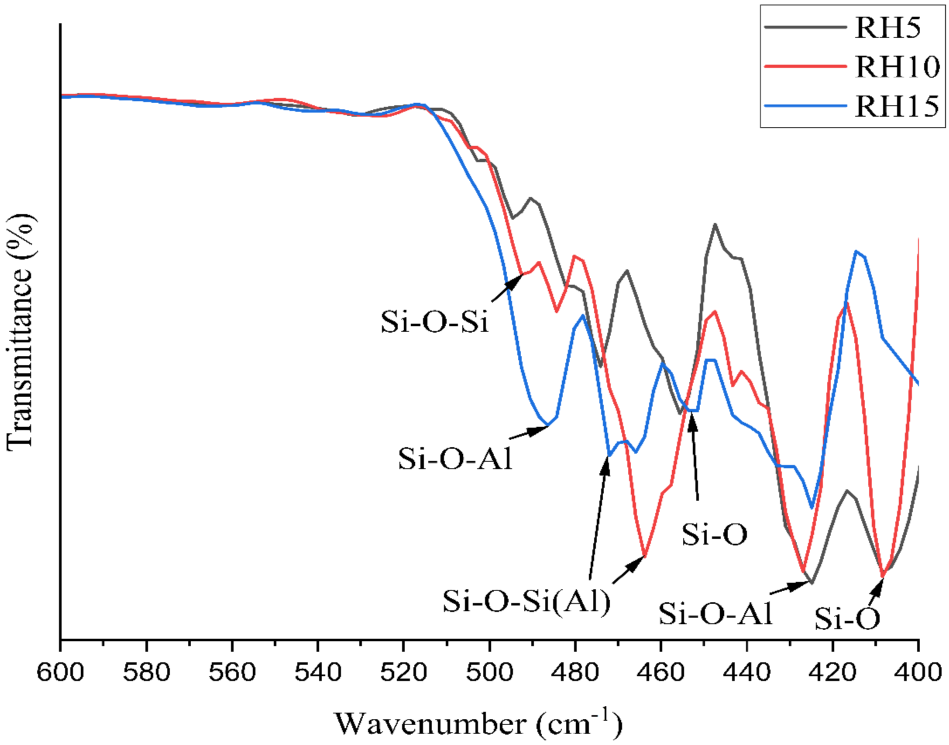

Figure 4.10: FTIR spectra of geopolymer samples with RHA.

The FTIR spectra presented in Figure 4.10 provide a detailed analysis of the structural evolution and bond formation in geopolymer matrices incorporating varying amounts of rice husk ash (RHA), specifically RH5, RH10, and RH15, corresponding to 5%, 10%, and 15% addition levels, respectively. In the RH5 sample, sharp and distinct peaks at 494 cm^{-1} and 474 cm^{-1} correspond to Si–O–Si and Si–O–Si(Al) asymmetric stretching vibrations, respectively, indicating a highly polymerised and well-connected silicate network with effective aluminium incorporation into the gel matrix. The pronounced peaks at 455 cm^{-1} and 424 cm^{-1}, associated with Si–O bending and Si–O–Al bending vibrations, further confirm the formation of a stable and cross-linked aluminosilicate gel. In comparison, the broad peak at 408 cm^{-1} suggests a minor presence of disordered or incomplete reaction products. As the RHA content increases to RH10, the spectrum shows a wider and weaker Si–O–Si stretching peak at 492 cm^{-1}, reflecting a decline in network connectivity and the onset of structural disorder. The sharp peak at 484 cm^{-1} and the intense peak at 463 cm^{-1}, corresponding to Si–O–Si(Al) and Si–O–Al asymmetric stretching, indicate moderate aluminium incorporation but with increasing bond distortion and partial breakdown of the aluminosilicate framework. Strong and broad peaks at 426 cm^{-1} and 408 cm^{-1} in RH10 highlight the dominance of amorphous phases and incomplete polymerisation. In the RH15 sample further broadening and intensity reduction at 486 cm^{-1} and 472 cm^{-1} reveal poor silicate network formation and strained Si–O–Si and Si–O–Si(Al) bonding environments. Peaks at 465 cm^{-1} and 453 cm^{-1}, though still present, exhibit reduced intensity, indicating weakened aluminosilicate connectivity, while broad and deep peaks at 424 cm^{-1} confirm the prevalence of disordered structures and highly amorphous phases at higher RHA content, which may adversely affect the mechanical performance and durability of the resulting geopolymer matrix.

iii) FTIR of NH, DE5, and RH5 Geopolymer Samples.

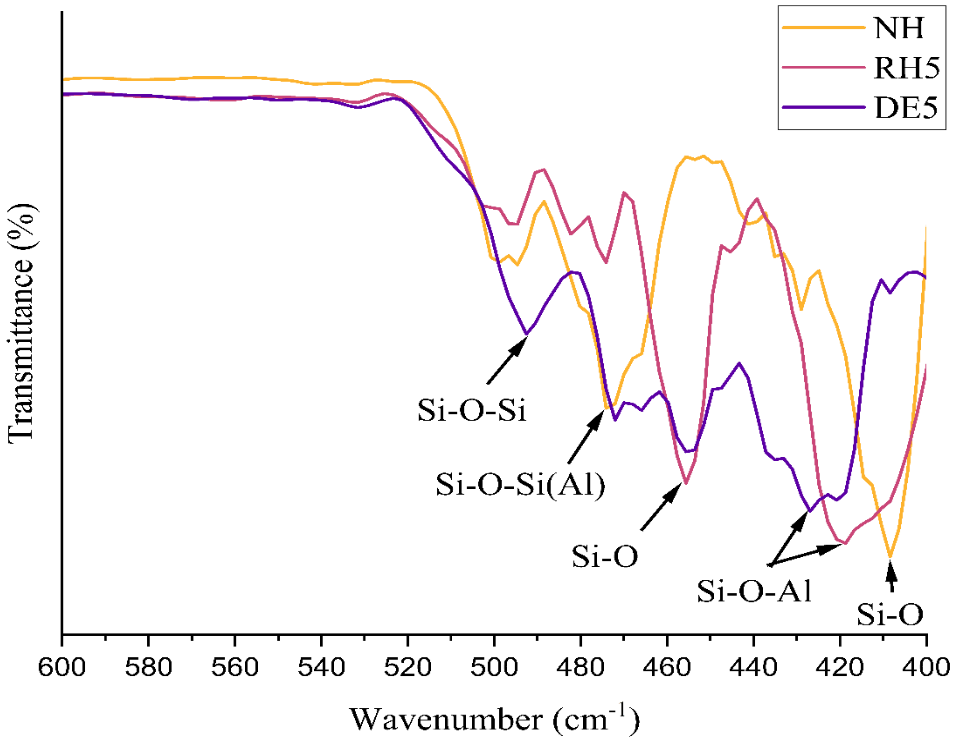

Figure 4.11: FTIR spectra of NH, DE5, and RH5.

The FTIR spectral analysis presented in Figure 4.11 demonstrates the evolution of the aluminosilicate gel network in samples NH, RH5, and DE5. In the NH sample, the broad and shallow band at 494 cm^{-1} indicates initial Si–O–Si asymmetric stretching linked to early gel network formation, while the sharp and intense peak at 474 cm^{-1} confirms the presence of Si–O–Si(Al) bonds with moderate aluminium substitution, suggesting moderate polymerisation of the silicate framework. A sharp but shallow peak at 428 cm^{-1} indicates the formation of weak Si–O–Al bonds, while the highly intense band at 408 cm^{-1} corresponds to disordered Si–O bending vibrations, highlighting the presence of an incomplete and poorly developed aluminosilicate gel structure. The RH5 sample exhibits an enhanced silicate network, as evidenced by the stronger peak at 494 cm^{-1} and a sharp, deep peak at 474 cm^{-1}, indicating effective aluminium incorporation and a highly polymerised structure. The sharp peak at 455 cm^{-1} and deep absorption at 424 cm^{-1} further confirm the strong Si–O bending and increased formation of Si–O–Al bonds, though disordered structures are still detected.

In contrast, the DE5 sample demonstrates a more advanced gel network, with a moderately broad peak at 492 cm^{-1} confirming ongoing Si–O–Si bond formation and the sharp peak at 472 cm^{-1} indicating a highly polymerised silicate framework. The pronounced peak at 467 cm^{-1} reflects vigorous Si–O–Al asymmetric stretching, signifying adequate aluminium substitution into the network. Well-defined peaks at 453 cm^{-1} and 437 cm^{-1} indicate robust Si–O bending and moderate Al incorporation, contributing to network strength. However, broad and shallow bands at 428 cm^{-1} and 406 cm^{-1} highlight areas of residual disorder and incomplete reaction products. These results suggest that DE5 exhibits the most developed and polymerised aluminosilicate framework among the samples, followed by RH5. At the same time, NH remains at an early stage of gel network development with significant structural disorder.

4.2.5 FESEM, EDS and Elemental mapping

Figures 4.12 to 4.18 show the microstructure and elemental mapping of NH, DE, and RHA-based geopolymer samples.

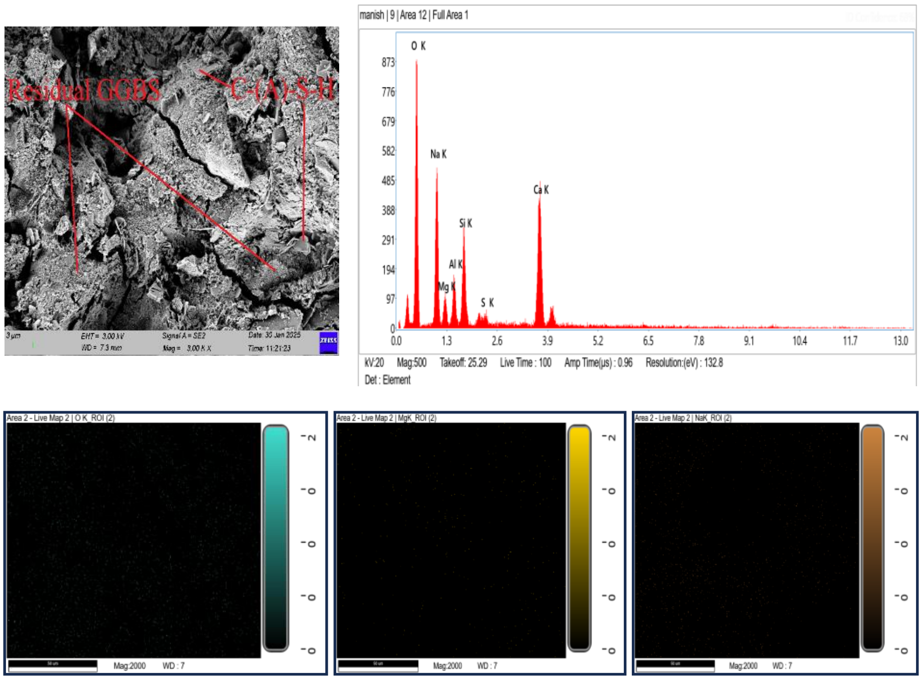

Figure 4.12: FESEM image, EDS spectrum, and elemental mapping of NH.

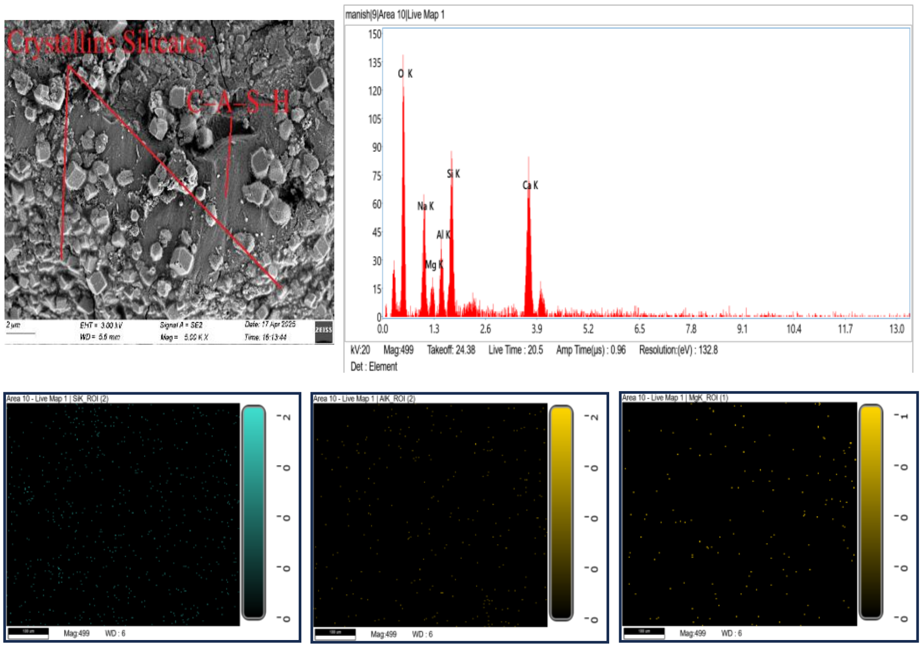

Figure 4.13: FESEM image, EDS spectrum, and elemental mapping of DE5.

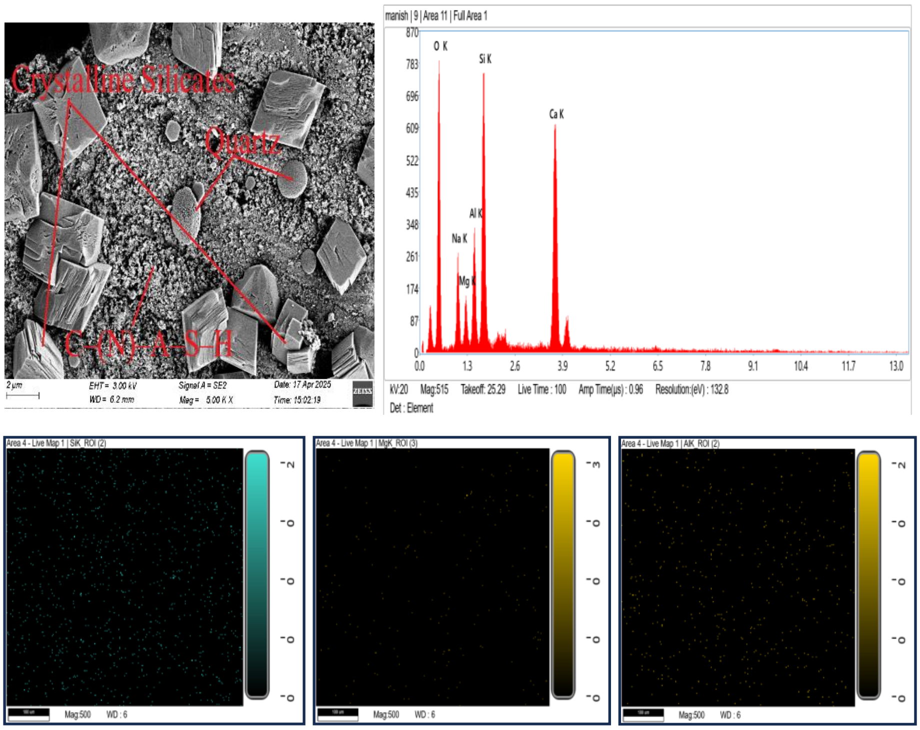

Figure 4.14: FESEM image, EDS spectrum, and elemental mapping of DE10.

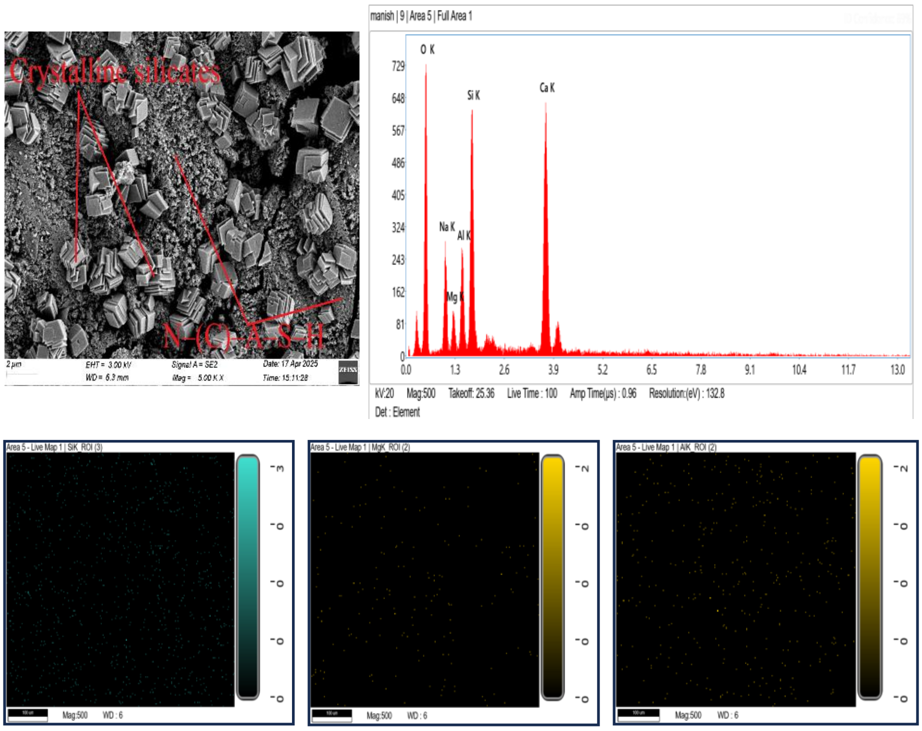

Figure 4.15: FESEM image, EDS spectrum, and elemental mapping of DE15.

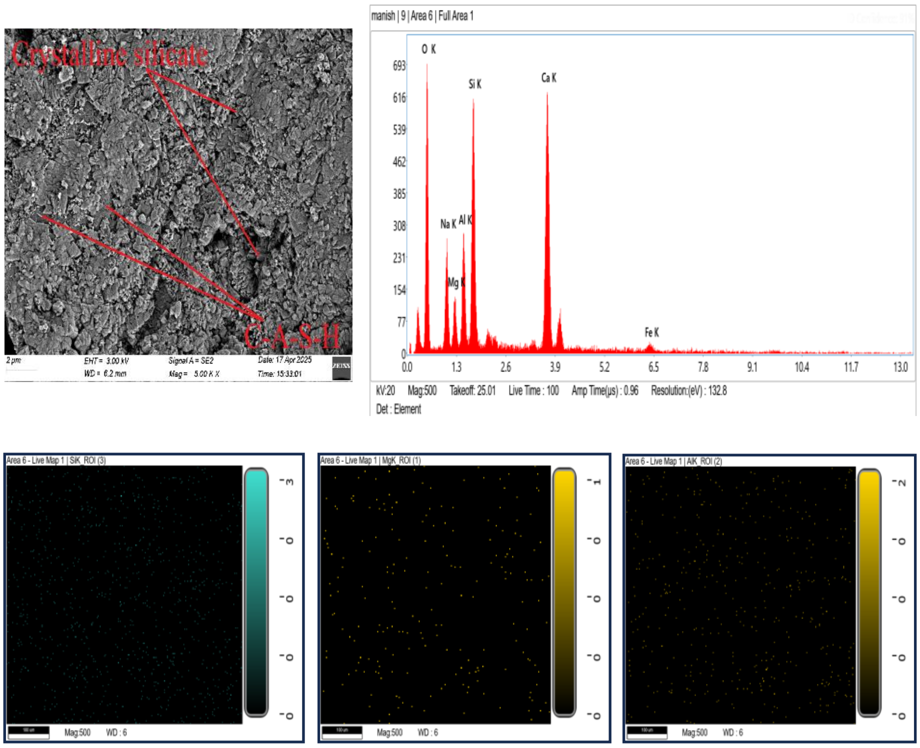

Figure 4.16: FESEM image, EDS spectrum, and elemental mapping of RH5.

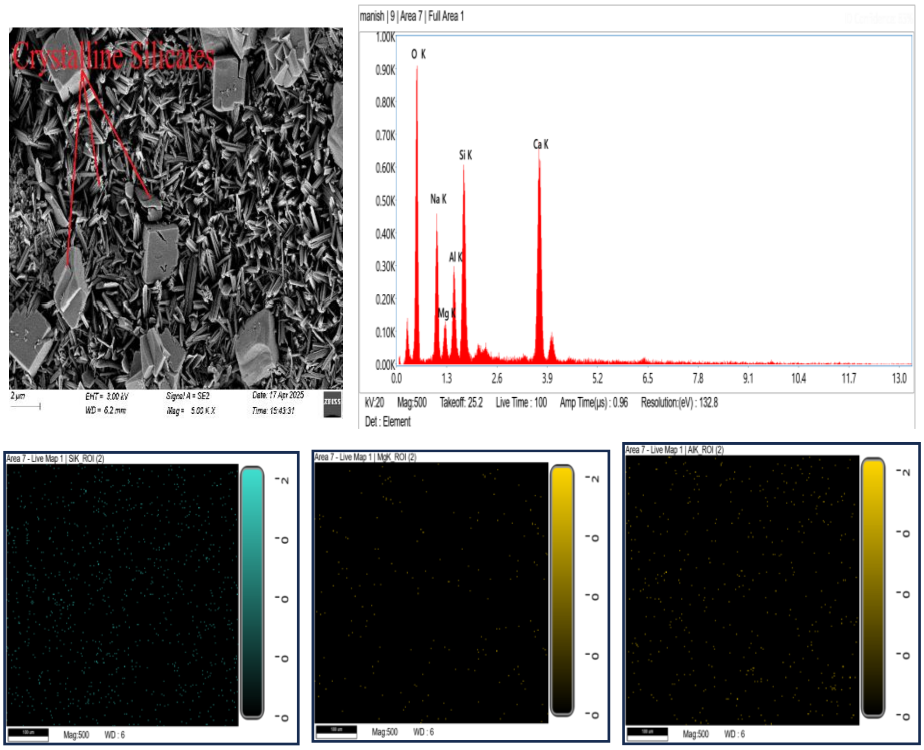

Figure 4.17: FESEM image, EDS spectrum, and elemental mapping of RH10.

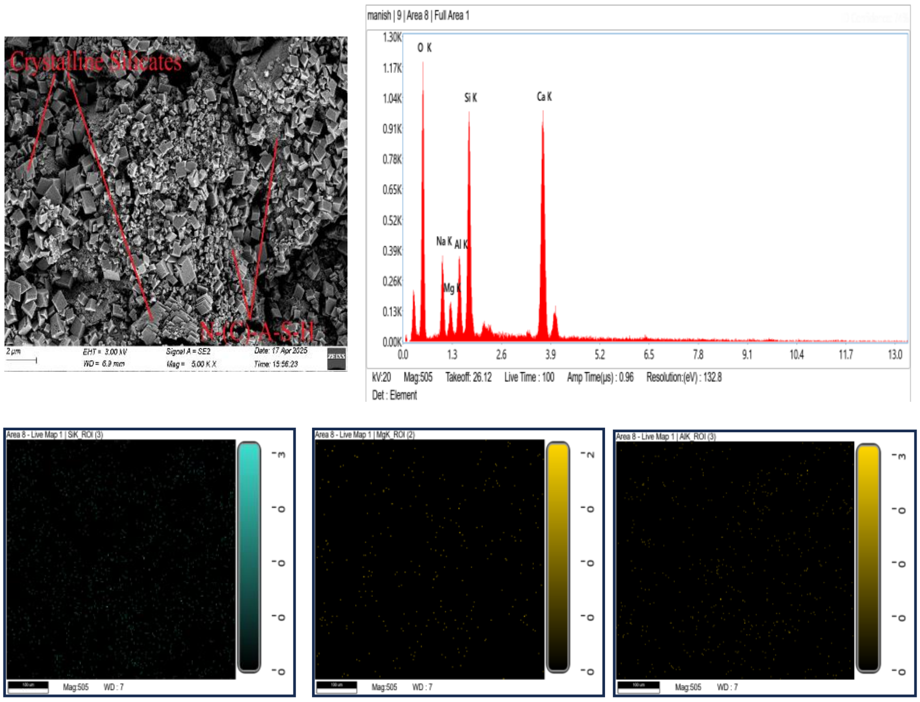

Figure 4.18: FESEM image, EDS spectrum, and elemental mapping of RH15.

The FESEM analysis of the NH sample shows a heterogeneous, poorly densified matrix with a rough, fractured surface populated by large flaky platelets and irregular granular agglomerates. These flaky platelets and agglomerates indicate partially reacted GGBS and a largely amorphous aluminosilicate matrix, possibly containing early-stage C-(A)-S-H gel. Significant porosity and prominent macro-cracks with branching micro-cracks reflect incomplete polymerisation and weak gel cohesion, indicative of a largely amorphous matrix with scattered crystalline inclusions, possibly underdeveloped C-(A)-S-H phases. For the DE series, DE5 exhibits a uniform and compact microstructure with well-formed cubic and polygonal crystals, identified as crystalline silicates such as Na-A zeolite, featuring tight interlocking particle arrangements and minimal porosity, indicating effective geopolymerization. DE10 presents a poorly compacted matrix characterised by wide shrinkage cracks, scattered crystalline phases including crystalline silicates such as Na-A, Na-P1 and rough-surfaced spherical particles (quartz); the matrix shows less pure C–A–S–H formation and instead suggests the presence of C–N–A–S–H gel, and poor bonding. DE15 exhibits the highest porosity and heterogeneity, with large flat crystalline plates and pseudo-cubic particles of Na-P1—representing zeolitic crystallisation from excess unreacted silica and sodium aluminosilicates—more N–A–S–H formation is visible, which results in a more porous structure and a mechanically weak, highly porous matrix. In the RHA series, RH5 reveals a dense and compact microstructure with pseudo-cubic crystals tightly stacked and terrace-like faceted—representing well-formed crystalline silicates such as Na-A or Na-P1 zeolites—minimal porosity, and well-developed particle bonding dominated by more C–A–S–H formation. RH10 shows a heterogeneous, highly porous microstructure dominated by acicular (needle-like) crystals—identified as Na-P1 zeolite like crystalline silicates—creating a reticulated porous network, with coexisting flat and pseudo-cubic crystalline phases such as residual silica and early crystalline zeolites, reflecting silica supersaturation and the formation of secondary crystalline products rather than a continuous gel network; C–A–S–H or N–A–S–H phases are not visible. RH15 displays a highly refined and compact matrix dominated by fine equiaxed pseudo-cubic crystals—indicating advanced crystalline silicate formation, potentially Na-A and Na-P1 type phases—minimal interconnected porosity, and no significant cracks, suggesting a structurally stable, highly crystalline matrix with dominant N–A–S–H formation..

EDS spectra of NH show strong, balanced Si and Al peaks and a notable Mg presence, indicating a fully reacted slag-based matrix with no residual precursors. DE5 displays a dominant Si peak due to added diatom silica, moderate Al and Mg peaks, and minor indications of unconsumed diatom structures. DE10 shows an even stronger Si peak, reduced Al content, and signs of residual quartz or amorphous silica, confirming incomplete conversion of DE. DE15 exhibits the highest Si content with weak Al and Mg signals, indicating significant residual unreacted silica and extremely limited geopolymerization. RH5 shows a higher Si/Al ratio in the RHA series than NH, with strong Si and Al peaks and moderate Mg, indicating effective incorporation of RHA-derived reactive silica into the binder. RH10 exhibits a further increase in the Si/Al ratio, indicating excessive silica replacement of slag and reduced gel connectivity. RH15 presents the highest Si intensity among RHA samples, reflecting maximised silica incorporation and minimal remaining amorphous gel, with Al and Mg signals significantly reduced.

Elemental mapping of NH reveals uniform distributions of Si, Al, and Mg across the matrix, confirming a continuous and homogeneous aluminosilicate distribution. DE5 shows moderately uniform Si, Al, and Mg distributions, with localised Si-rich regions at diatom relics, indicating partial heterogeneity. DE10 exhibits highly non-uniform Si mapping with bright silica-rich clusters corresponding to unreacted diatom residues, and more continuous but lower intensity Al and Mg distributions in the sparse gel phase. DE15 presents stark contrasts, with strong Si localisation around diatom remnants and scattered Al and Mg in the sparse binder, confirming poor matrix integration. In RH5, elemental maps show a uniform distribution of Si, Al, and Mg, indicating thorough dispersion of reaction products. RH10 mapping is relatively homogeneous but highlights silicon enrichment along the needle-like crystalline structures, with aluminium and magnesium following similar patterns. RH15 shows uniform elemental distribution, confirming maximum incorporation of RHA-derived silica and a dense, compositionally consistent binder.

Chapter 5

DISCUSSION

The inclusion of diatomaceous earth (DE) or rice husk ash (RHA) as alternative silica sources in the activator solution significantly influenced the mechanical and physical properties of the geopolymer. As the data in Figure 4.4 shows, 5% substitutions (DE5, RH5) yielded the highest compressive strengths, whereas 10% and 15% substitutions led to strength reductions. Specifically, DE5 attained 34.85 MPa at 28 d (versus 23.09 MPa for the silicate-free control NH), and RH5 reached 27.05 MPa. In both series, the trend was similar: 5% DE/RHA improved strength, indicating optimal dissolution of silica and enhanced formation of a dense, continuous C–A–S–H gel network, but 10% and 15% additions gave lower strength (i.e., DE15 = 21.67 MPa, RH15 = 13.15 MPa). Thus, incorporating 5% DE/RHA enhanced the silica content and promoted early geopolymerization; however, higher dosages led to a reduction in material strength. These results are in line with the findings of previous studies. Font et al. [14] demonstrated that using residual diatomaceous earth as an alternative silica source in fly ash-based geopolymers resulted in compressive strengths of approximately 20 MPa, which was around 20% lower than those achieved with commercial sodium silicate (~25 MPa), while Felaous et al. [15] reported that ambient-cured GGBS with 10% DE (8 M NaOH) reached ~42 MPa. Similarly, Mulapeer and Omar [65] showed that using RHA-derived activators under ambient curing increased compressive strength by 35% at 28 days, confirming RHA's effectiveness as a silica alternative. Yamini J. Patel et al. [66] also found that RHA addition enhanced the mechanical and fracture properties of GGBFS-based geopolymer concrete. However, excessive RHA reduces strength due to higher porosity and crystalline by-products. The lower relative strength observed for DE5 and RH5 may be due to differences in activator concentration or raw material reactivity; however, the general pattern, with a maximum at 5% followed by a decline, is consistent with previous studies.

The physical properties of the geopolymer also decreased with silica addition. Bulk density decreased from 1.98 g/cm³ (NH) to 1.84 g/cm³ (DE15) and 1.77 g/cm³ (RH15) shown in Figure 4.5(a). As shown in Figure 4.5(b), both water absorption and porosity increased with the addition of DE and RHA. The control mix (NH) showed the lowest values (0.38% water absorption and 0.76% porosity), while DE15 exhibited 4.60% water absorption and 7.23% porosity. The highest values were observed for RH15, with 8.00% water absorption and 13.10% porosity. At an additional level of 15%, RHA resulted in higher porosity (13.1%) compared to DE, which exhibited lower porosity (7.2%). The higher absorption/porosity with RHA is attributed to its inherently porous ash structure and the formation of more capillary voids. These trends explain part of the strength differences: a more porous, lower-density matrix (as in RH10/15) will inherently be weaker. The fact that DE5 and RH5 also had slightly lower density but still higher strength indicates that at low amounts, the additional silica helped densify the gel network, whereas higher quantities introduced defects.

X-ray diffraction confirms extensive geopolymer gel formation in all samples (Figure 4.7, 4.8, 4.9). In both DE- and RHA-modified binders, new broad humps between ~25–35°2θ appeared, indicating amorphous aluminosilicate gel. Sharp new peaks at ~7.12°, 29.21°, and 49.44°2θ correspond to calcium-aluminosilicate-hydrate (C–A–S–H) gel [67]. Peaks at 11.44°, 23.2°, and 34.82°2θ indicate hydrotalcite (a Mg–Al layered double hydroxide). Hydrotalcite formation is typically observed in high-Ca/Mg slags, as reported in previous studies [67]. In DE mixes, the residual quartz peak (26.6–27°) remained visible in DE10 and DE15, showing unreacted silica (Figure 4.7). Whereas none of the RHA mixes showed this peak, RHA ash was amorphous primarily. This implies that beyond 5% DE, the crystalline silica present in DE was not fully dissolved. The XRD patterns suggest that a moderate amount of DE or RHA promotes the formation of the desired C–A–S–H and hydrotalcite gel network, as indicated by the intensified amorphous hump, while excessive additive leaves behind unused silica.

FTIR spectra reinforce these findings evident in Figures 4.10, 4.11, and 4.12. In the DE5 geopolymer, distinct Si–O–Si and Si–O–Al asymmetric stretch bands at ~472 cm^{-1} and 467 cm^{-1} were sharp and intense, indicating a highly polymerised aluminosilicate network with good Al incorporation. DE5 also showed defined Si–O bending modes 453 cm^{-1}, 437 cm^{-1}, indicative of extensive cross-linking. The spectra of DE10 and DE15 exhibit broad, attenuated peaks—particularly a weak and broad feature at 494 cm^{-1}—and persistent shoulders at 453 cm^{-1}, indicating increased structural disorder and the presence of unreacted silica. In the same manner, RH5 exhibited strong Si–O–Si and Si–O–(Si, Al) bands at ~494 and 474 cm^{-1} and pronounced bending vibrations (455, 424 cm^{-1}), reflecting a robust gel framework. As the RHA content increased to 10–15%, the peaks at 486 and 472 cm^{-1} became broader and less intense, while the amorphous band around 424 cm^{-1} became more prominent, as shown in Figure 4.11. The comparative FTIR spectra for NH, RH5, and DE5 (Figure 4.12) reveal that DE5 exhibits the sharpest and most polymerized peaks, RH5 shows intermediate features, and NH displays the weakest spectral characteristics. FTIR confirms that 5% addition of RHA/DE produces a complete silicate–aluminate gel network, while higher additions yield incomplete polymerisation, consistent with the lower strengths.

FESEM analysis provides a microstructural explanation for the mechanical performance of the control and modified geopolymer systems. The control sample (NH) exhibits a heterogeneous and poorly densified matrix containing large flaky particles and irregular granular agglomerates (Figure 4.13). These morphologies, attributed to partially reacted GGBS and a discontinuous amorphous C–(A)–S–H gel, are accompanied by macro- and micro-cracks, correlating with its moderate compressive strength of 23 MPa. Whereas, DE5 displays a highly compact and uniform microstructure with well-formed pseudo-cubic and polygonal crystals (Figure 4.14), identified as crystalline silicates such as Na-A zeolite. These densely packed particles indicate effective geopolymerization and near-complete reaction, consistent with the highest strength in this series (34.8 MPa). However, the matrix becomes less compact with 10% DE (Figure 4.15). Shrinkage cracks and increased porosity emerge, along with scattered crystalline silicates such as Na-P1 and partially reacted diatomite particles. These features reflect incomplete gel formation, transitioning toward a mixed C–(N)–A–S–H phase with weaker bonding. DE15 (Figure 4.16) exhibits the most porous and heterogeneous structure, dominated by large flat plate-like crystals and spherical granular relics of unreacted diatomite. The formation of coarse Na-P1-type phases and poor gel continuity explains the pronounced drop in strength to 21.7 MPa.

The RHA series reveals similar trends. RH5 (Figure 4.17) presents a dense, well-bonded microstructure with tightly packed pseudo-cubic and terrace-like crystalline silicates, resembling Na-A or Na-P1 zeolites, embedded in a C–A–S–H rich matrix. This structure supports its superior mechanical performance. In RH10 (Figure 4.18), the matrix becomes highly porous and heterogeneous, with acicular (needle-like) crystals forming a reticulated framework alongside flat and pseudo-cubic phases. These acicular structures, likely corresponding to zeolite or hydrotalcite-like silicates, indicate silica oversaturation and the precipitation of crystalline by-products rather than the formation of a continuous binding gel. As a result, structural cohesion deteriorates. RH15 (Figure 4.19) unexpectedly exhibits a more compact surface morphology, characterised by fine equated pseudo-cubic crystals and reduced visible porosity. However, the dominance of crystalline silicate phases (Na-A and Na-P1) over amorphous gel phases like N–A–S–H limits strength development, resulting in a low compressive strength of 13.2 MPa. The FESEM observations confirm that the optimal microstructure, characterized by a dense, well-bonded matrix dominated by amorphous aluminosilicate gel, occurs only at low additive contents (5%) At higher levels of DE or RHA, the increased formation of N–A–S–H gel, the presence of unreacted particles, secondary crystalline silicates, shrinkage-induced cracking, and the development of voids collectively reduce the effectiveness of the gel network, which is reflected in the compromised mechanical performance.

Energy-dispersive analysis further clarifies the chemistry.

The NH matrix has balanced Si and Al signals with some Mg (from GGBS) (Figure 4.13), indicating a fully reacted C–A–S–H–type gel. DE5 shifts the Si/Al ratio upward: Si peak dominates but Al and Mg remain moderate (Figure 4.14), consistent with effective DE integration. At DE10 and DE15, the Si peak grows very large while Al and Mg diminish (Figure 4.15), confirming that much DE silica remained unreacted (indeed, EDS still sees quartz) and the aluminosilicate gel is limited. In the RHA series, Si/Al similarly rises with more RHA: RH5 shows higher Si/Al than NH (Figure 4.16), RH10 even more, and RH15 has the highest Si intensity with very weak Al/Mg (Figure 4.17). This indicates that at >5% RHA, the additional silica displaces slag (Al source) without fully forming C–A–S–H gel, reducing the binder network connectivity.

Elemental mapping highlights this contrast: DE10 and DE15 have localised bright Si-rich regions (unreacted DE) with scattered Al/Mg (Figure 4.15, 4.16), whereas RH samples maintain relatively uniform Si, Al, Mg maps (especially RH15) (Figure 4.19). This suggests that RHA dissolves more uniformly, while DE leaves heterogeneous residues.

Taken together, the microstructural observations explain the strength trends. The highest strengths (DE5, RH5) correspond to maximally developed C–A–S–H gel networks: intense amorphous XRD halo, sharp Si–O–Si/Al bonds in FTIR, and compact FESEM morphology. In contrast, DE10/15 and RH10/15 show evidence of unincorporated silica (XRD quartz peaks, broad FTIR bands) and poor connectivity (FESEM cracks, high porosity). This aligns with the established understanding that aluminosilicate binding gels strengthen the matrix, whereas excess non-gel silica or crystalline phases act as defects [67]. In particular, the formation of needle-like crystalline phases in RH10 and RH15 (seen in FESEM) indicates silica oversaturation leading to zeolitic or calcite products rather than amorphous C–A–S–H, consistent with the steep strength decline. Hydrotalcite peaks in XRD and Mg in EDS demonstrate that part of the binder includes this layered double hydroxide, which can further densify the matrix [16, 67]. The observed optimal dosage (~5%) likely reflects the slag system's ideal Si/Al ratio. The added reactive silica supplements the slag at low additive levels to promote more complete gelation and cross-linking. Literature suggests that moderate Si/Al (often ~2) is favourable for geopolymer gel stability [18, 67]. Beyond this optimum, the Si/Al ratio becomes too high, as our EDS data show, and the excess silica is not incorporated into the gel matrix. This "silica overdose" phenomenon (also noted by Cheng et al. [18]) destabilises the geopolymer structure and enhances porosity, consequently weakening the material. In this study, 10–15% additive exceeds the system's capacity to consume the silica: unreacted quartz (DE) and amorphous RHA particles remained, and cracks and pores proliferated, undermining the microstructure. Similar overdosage effects have been reported in alkali-activated systems, where additional fine silica initially accelerates reaction but ultimately yields diminishing returns [20, 67]. In summary, DE and RHA can serve as partial silica sources for ambient-cured GGBS geopolymers, but their efficacy differs. DE5 achieved the highest strength of our mixes, likely due to the efficient formation of a dense C–A–S–H gel (as supported by XRD/FTIR/FESEM) and a favourable Si/Al ratio. RHA5 also improved strength, but to a lesser extent, possibly because RHA's high amorphous silica content accelerated early reaction but also introduced more inherent porosity (Figure 4.5(b)). In both series, 5% was optimal: it enhanced geopolymerization (more gel, less porosity) relative to the control. However, at 10–15% addition, both additives caused strength losses. DE beyond 5% contributed excess crystalline silica that did not dissolve entirely. RHA beyond 5% led to silica super saturation, forming secondary crystals (FESEM) and a weaker gel network. These findings align with prior studies of alternative activators in slag geopolymers. For example, ambient-curing GGBS activated with 10% DE (8 M NaOH) has been shown to form the same amorphous C–A–S–H gel as with sodium silicate, achieving ~42 MPa [15]. The lower result at 10% DE likely reflects the higher NaOH concentration and possibly different DE quality. Likewise, in metakaolin-based systems, RHA/NaOH solutions have been reported to replace waterglass effectively [16], and the use of slaked lime has been shown to further enhance the reactivity of natural pozzolans in geopolymer synthesis [67], in line with our observation that RH5 produced a robust gel. The present data, therefore, extend these insights to slag systems: waste silica sources can partially substitute commercial silicate, but only up to an optimal content. Too much additive leads to gel saturation and defects at the microscale, as our XRD/FTIR/FESEM captured. Thus, the study confirms that DE and RHA (5% each) can enrich slag geopolymers with additional Si to strengthen the C–A–S–H network, the geopolymer structure becomes destabilised and porosity increases, which in turn reduces the strength of the material. The negative impacts of too much silica have been noted in the literature on geopolymers [18, 67].

Chapter 6

CONCLUSION

This study has demonstrated that replacing commercial waterglass with silica from rice husk ash (RHA) or diatomaceous earth (DE) can yield geopolymer binders with satisfactory strength and microstructure. The optimal formulations were obtained at just 5 % of each alternative silica source: 5% DE produced a 28-day compressive strength of 34.85 MPa, and 5% RHA gave 27.05 MPa. These values compare with conventional alkali-activated slag binders, indicating that small additions of RHA or DE are sufficient to supply extra silica for network formation. In contrast, higher additions (10–15%) significantly reduced strength. This reduction results from excess SiO_2 that remains unreacted or dissolves without contributing effectively to the primary gel structure. In other words, beyond the optimum dosage, too much reactive silica leads to incomplete geopolymer network formation and increased porosity, while also promoting secondary phase formation such as N–A–S–H gel and zeolitic crystals, which disrupt the continuity of the C–A–S–H network and diminish overall strength, as confirmed by FESEM.

X-ray diffraction and spectroscopy results support this interpretation. At 5 % substitution, the XRD patterns revealed the typical calcium–aluminosilicate hydrate (C–A–S–H) gel and hydrotalcite phases characteristic of slag-based geopolymers. The FTIR spectra of the 5 % mixes showed sharp Si–O–Si/Al peaks, indicating a well-polymerised aluminosilicate network. In contrast, 10–15 % mixtures showed broader, attenuated Si–O bands and noticeable residual quartz peaks, confirming incomplete reaction. FESEM micrographs likewise showed that the 5 % RHA/DE samples had a dense, compact matrix, whereas the high-addition mixes contained many pores, and secondary bond formation dominated. These observations are consistent with known geopolymer chemistry. When the Si/Al ratio is too high, excess silica fails to integrate into the framework and instead remains as an undissolved phase.

The findings validate the technical feasibility of partial RHA/DE replacement of sodium silicate. The optimised 5 % blends achieved compressive strengths in the 30–35 MPa range, suitable for many civil-engineering applications. This agrees with prior work showing that industrial by-products like rice husk ash and spent diatomite can act effectively as silica sources, producing geopolymer binders with good mechanical properties (e.g. ~38 MPa at long term) and added environmental benefits. In summary, replacing a fraction of waterglass with finely milled RHA or DE is a viable strategy to lower costs and CO_2 footprint, without compromising the integrity of the alkali-activated slag binder. The C–A–S–H and hydrotalcite reaction products observed here also confirm that the high-calcium system follows the expected hardening chemistry of alkali-activated slag.

Chapter 7

FUTURE SCOPE

The next phase of this research aims to scale up the work from past-level studies to concrete-level applications. Future work will incorporate the developed RHA/DE–GGBS geopolymer mortar into concrete mixes by blending with fine and coarse aggregates. This step will enable the evaluation of fresh properties such as workability and setting behaviour, as well as hardened properties like compressive, tensile, and flexural strength. Researchers can cast pilot-scale structural elements such as beams, columns, and slabs using the developed geopolymer concrete to assess its practical feasibility and structural performance in real-life conditions.

Further investigations should focus on optimising the activator design. Researchers should explore the influence of varying NaOH concentrations and NaOH-to-sodium silicate ratios on the reactivity and mechanical properties of the geopolymer system. Future studies can achieve complete silica dissolution and improved polymerisation by increasing the Na_2O content and activator molarity beyond 10 M and incorporating soluble silicates. These modifications can enhance mechanical strength and affect microstructural properties.

Additionally, combining RHA and DE or introducing other regionally available industrial and agricultural wastes could generate synergistic effects. These effects may arise from the diversity in particle morphology and chemical reactivity, improving packing density and overall performance compared to systems based on a single activator.

To ensure long-term viability, researchers should assess durability under aggressive environmental conditions, including sulfate and chloride attack, acid exposure, carbonation, and freeze-thaw cycles. Analysing microstructural and transport properties, such as porosity, permeability, and alkali leaching, will help validate the material's structural integrity under realistic service conditions.

Finally, conducting a thorough techno-economic and life cycle assessment (LCA) is crucial. These evaluations will benchmark the developed geopolymer materials' cost efficiency and carbon footprint against conventional cementitious systems. By doing so, researchers can support the broader adoption of low-carbon, high-performance geopolymer concretes, especially in regions rich in agricultural and mineral waste resources.

Chapter 8

REFERENCES

[1] R. M. Andrew, “Global CO2 emissions from cement production, 1928-2018,” *Earth Syst Sci Data*, vol. 11, no. 4, pp. 1675–1710, Nov. 2019, doi: 10.5194/ESSD-11-1675-2019,.

[2] P. Cong and Y. Cheng, “Advances in geopolymer materials: A comprehensive review,” *Journal of Traffic and Transportation Engineering (English Edition)*, vol. 8, no. 3, pp. 283–314, 2021, doi: 10.1016/j.jtte.2021.03.004.

[3] J. L. Provis and J. S. J. van Deventer, *Geopolymers: Structure, Processing, Properties and Industrial Applications*. Woodhead Publishing, 2009.

[4] D. Hardjito and B. V Rangan, “Development and Properties of Low-Calcium Fly Ash-Based Geopolymer Concrete,” 2005.

[5] A. Palomo and others, “Alkali-activated fly ashes: A cement for the future,” *Cem Concr Res*, vol. 29, no. 8, pp. 1323–1329, 1999, doi: 10.1016/S0008-8846(99)00154-3.

[6] J. J. Kipsanai, P. M. Wambua, S. S. Namango, and S. Amziane, “A Review on the Incorporation of Diatomaceous Earth as a Geopolymer-Based Concrete Building Resource,” *Materials (Basel)*, vol. 15, no. 20, p. 7130, 2022, doi: 10.3390/ma15207130.

[7] L. K. Turner and F. G. Collins, “Carbon dioxide equivalent (CO_2-e) emissions: A comparison between geopolymer and OPC cement concrete,” *Constr Build Mater*, vol. 43, pp. 125–130, 2013, doi: 10.1016/j.conbuildmat.2013.01.023.

[8] P. Duxson and J. S. J. van Deventer, “Geopolymer technology: The current state of the art,” *J Mater Sci*, vol. 42, no. 9, pp. 2917–2933, 2007, doi: 10.1007/s10853-006-0637-z.

[9] H. U. Ahmed and others, “Compressive Strength of Sustainable Geopolymer Concrete Composites: A State-of-the-Art Review,” *Sustainability*, vol. 13, p. 13502, 2021, doi: 10.3390/su132413502.

[10] S. S. Mohapatra, J. Mishra, B. Nanda, and S. K. Patro, “A Review on Waste-Derived Alkali Activators for Preparation of Geopolymer Composite,” *Mater Today Proc*, vol. 56, pp. 440–446, 2022, doi: 10.1016/j.matpr.2022.01.400.

[11] Saloni *et al.*, “Performance of Rice Husk Ash-Based Sustainable Geopolymer Concrete with Ultra-Fine Slag and Corn Cob Ash,” *Constr Build Mater*, vol. 279, p. 122526, 2021, doi: 10.1016/j.conbuildmat.2021.122526.

[12] B. Nanda, J. Mishra, and S. K. Patro, “Synthesis of Rice Husk Ash Based Alkaline Activators for Geopolymer Binder Systems: A Review,” *Journal of Building Engineering*, vol. 91, p. 109694, 2024, doi: 10.1016/j.jobe.2024.109694.

[13] L. Handayani, S. Aprilia, M. M. A. B. Abdullah, I. Hussain, and M. I. Ahmad, “Synthesis of Sodium Silicate from Rice Husk Ash Using Thermal Method,” *J Phys Conf Ser*, 2021, doi: 10.1088/1742-6596/1845/1/012072.

[14] A. Font *et al.*, “Use of Residual Diatomaceous Earth as a Silica Source in Geopolymer Production,” *Mater Lett*, vol. 223, pp. 10–13, 2018, doi: 10.1016/j.matlet.2018.04.010.

[15] K. Felaous, A. Aziz, and M. Achab, “Physico-mechanical and durability properties of new eco-material based on blast furnace slag activated by Moroccan diatomite gel,” *Environmental Science and Pollution Research*, vol. 30, pp. 3549–3561, 2023, doi: 10.1007/s11356-022-22461-7.

[16] E. Kamseu and others, “Substitution of sodium silicate with RHA-NaOH solution in metakaolin-based geopolymer cement,”

J Clean Prod, vol. 142, pp. 3050–3060, 2017, doi: 10.1016/j.jclepro.2016.10.174.

[17] A. Aziz and others, “Effect of blast-furnace slag on physicochemical properties of pozzolan-based geopolymers,” *Mater Chem Phys*, vol. 258, p. 123880, 2021, doi: 10.1016/j.matchemphys.2020.123880.

[18] Y. Cheng and others, “Silica fume-derived activator as water glass substitute in fly ash geopolymer,” *Journal of Building Engineering*, vol. 51, p. 104228, 2022, doi: 10.1016/j.jobe.2022.104228.

[19] T. Luukkonen and others, “One-part alkali-activated materials: A review,” *Cem Concr Res*, vol. 103, pp. 21–34, 2018.

[20] A. H. Oti and others, “Pumice-derived sodium silicate for sustainable geopolymers,” *Constr Build Mater*, vol. 368, p. 130446, 2024.

[21] R. Roy, “A Comprehensive Analysis on Geopolymer Concrete in Reducing Carbon Dioxide Emissions,” 2020.

[22] K. Neupane and others, “Environmental sustainability of one-part geopolymer binders,” *J Clean Prod*, vol. 334, p. 130186, 2022.

[23] K. L. Scrivener, V. M. John, and E. M. Gartner, “Eco-efficient cements: Potential economically viable solutions for a low-CO_2 cement-based materials industry,” *Cem Concr Res*, vol. 114, pp. 2–26, 2018.

[24] M. Antoni, J. Rossen, F. Martirena, and K. Scrivener, “Cement substitution by a combination of metakaolin and limestone,” *Cem Concr Res*, vol. 42, no. 12, pp. 1579–1589, 2012.

[25] E. Gartner and T. Sui, “Alternative cement clinkers,” *Cem Concr Res*, vol. 114, pp. 27–39, 2018.

[26] J. Davidovits, *Geopolymer Chemistry and Applications*. 2008.

[27] N. K. Lee and H. K. Lee, “Setting and mechanical properties of alkali-activated fly ash/slag concrete manufactured at room temperature,” *Constr Build Mater*, vol. 47, pp. 1201–1209, 2013.

[28] P. Zhang, X. Sun, F. Wang, and J. Wang, “Mechanical Properties and Durability of Geopolymer Recycled Aggregate Concrete: A Review,” *Polymers (Basel)*, vol. 15, p. 615, 2023, doi: 10.3390/polym15030615.

[29] J. Oti, B. O. Adeleke, F. X. Anowie, J. M. Kinuthia, and E. Ekwulo, “Mechanical Properties of a Sustainable Low-Carbon Geopolymer Concrete Using a Pumice-Derived Sodium Silicate Solution,” *Materials*, vol. 17, p. 1792, 2024, doi: 10.3390/ma17081792.

[30] U. N. E. P. (UNEP), “Sustainable Building and Construction: Facts and Figures,” 2016.

[31] I. E. Agency, “Technology Roadmap: Low-Carbon Transition in the Cement Industry,” *IEA Report*, 2018.

[32] J. L. Provis, “Alkali-activated materials,” *Cem Concr Res*, vol. 114, pp. 40–48, 2018.

[33] P. K. Mehta and P. J. M. Monteiro, *Concrete: Microstructure, Properties, and Materials*. McGraw-Hill Education, 2014.

[34] J. O. Ikotun and others, “Geopolymer cement in pavement applications,” *Constr Build Mater*, vol. 380, p. 130812, 2024.

[35] M. Cavalieri, P. L. Ferrara, C. Finocchiaro, and M. F. Martorana, “An Economic Analysis of the Use of Local Natural Waste: Volcanic Ash of Mt. Etna Volcano (Italy) for Geopolymer Production,” *Sustainability*, vol. 16, p. 740, 2024, doi: 10.3390/su16020740.

[36] M. F. M. Tahir, M. M. A. B. Abdullah, and others, “Potential of Industrial By-Products Based Geopolymer for Rigid Concrete

Pavement Application," *Constr Build Mater*, vol. 344, p. 128190, 2022, doi: 10.1016/j.conbuildmat.2022.128190.

[37] R. Sharmin and others, "Waste clay brick powder in geopolymers," *Constr Build Mater*, vol. 369, p. 130465, 2024.

[38] K. Chen, Q. Liu, B. Chen, S. Zhang, L. Ferrara, and W. Li, "Effect of Raw Materials on the Performance of 3D Printing Geopolymer: A Review," *Journal of Building Engineering*, vol. 84, p. 108501, 2024, doi: 10.1016/j.jobe.2024.108501.

[39] B. A. Lanjewar, R. Chippagiri, V. A. Dakwale, and R. V Ralegaonkar, "Application of Alkali-Activated Sustainable Materials: A Step towards Net Zero Binder," *Energies (Basel)*, vol. 16, p. 969, 2023, doi: 10.3390/en16020969.

[40] J. Matsimbe, M. Dinka, D. Olukanni, and I. Musonda, "Geopolymer: A Systematic Review of Methodologies," *Materials*, vol. 15, p. 6852, 2022, doi: 10.3390/ma15196852.

[41] P. Duxson and others, "The role of inorganic polymer technology in the development of green concrete," *Cem Concr Res*, vol. 37, no. 12, pp. 1590–1597, 2007.

[42] A. Wang, Y. Zheng, Z. Zhang, and others, "The Durability of Alkali-Activated Materials in Comparison with Ordinary Portland Cements and Concretes: A Review," *Engineering*, vol. 6, pp. 695–706, 2020, doi: 10.1016/j.eng.2019.08.019.

[43] M. Amran, A. Al-Fakih, S. H. Chu, and others, "Long-term durability properties of geopolymer concrete: An in-depth review," *Case Studies in Construction Materials*, vol. 15, p. e00661, 2021, doi: 10.1016/j.cscm.2021.e00661.

[44] L. S. Wong, "Durability Performance of Geopolymer Concrete: A Review," *Polymers (Basel)*, vol. 14, p. 868, 2022, doi: 10.3390/polym14050868.

[45] R. R. Samuvel, P. Arulraj, and N. Ananthan, “Nanomaterials in geopolymer composites: A review,” *Developments in the Built Environment*, 2022, doi: 10.1016/j.dibe.2022.100114.

[46] M. F. Mohd Tahir *et al.*, “Optimization of fly ash based geopolymer mix design using Taguchi method,” in *AIP Conference Proceedings*, 2019. doi: 10.1063/1.5118152.

[47] H. Šimonová, P. Bazan, B. Kucharczyková, and others, “Hybrid Geopolymer Composites Based on Fly Ash Reinforced with Glass and Flax Fibers,” *Applied Sciences*, vol. 14, p. 9787, 2024, doi: 10.3390/app14219787.

[48] N. B. Singh and B. Middendorf, “Geopolymers as an Alternative to Portland Cement: An Overview,” *Constr Build Mater*, vol. 237, p. 117455, 2020, doi: 10.1016/j.conbuildmat.2019.117455.

[49] W. K. W. Lee and J. S. J. van Deventer, “The effect of ionic contaminants on the early-age properties of geopolymers,” *Cem Concr Res*, vol. 32, no. 4, pp. 577–584, 2002.

[50] L. Tositti, G. Masi, P. Morozzi, A. Zappi, and M. C. Bignozzi, “Cleaner, sustainable, and safer: Green potential of alkali-activated materials in current building industry, radiological good practice, and a few tips,” *Constr Build Mater*, vol. 409, p. 133879, 2023, doi: 10.1016/j.conbuildmat.2023.133879.

[51] I. E. Agency, “Roadmap for low-carbon cement technologies,” 2023.

[52] M. Schneider, M. Romer, M. Tschudin, and H. Bolio, “Sustainable cement production—present and future,” *Cem Concr Res*, vol. 41, no. 7, pp. 642–650, 2011, doi: 10.1016/j.cemconres.2011.03.019.

[53] N. Pattanayak, H. K. Behera, and S. S. Das, “Mix Design Strategy and Optimization Considering Characteristic Evaluation of

Geopolymer Concrete," *Journal of Building Engineering*, vol. 91, p. 109557, 2024, doi: 10.1016/j.jobe.2024.109557.

[54] R. Robayo-Salazar, J. Mejía-Arcila, R. M. de Gutiérrez, and E. Martínez, "Life Cycle Assessment of an Alkali-Activated Binary Concrete Based on Natural Volcanic Pozzolan: A Comparative Analysis to OPC Concrete," *Constr Build Mater*, vol. 176, pp. 103–111, 2018, doi: 10.1016/j.conbuildmat.2018.05.017.

[55] A. García-Díaz, S. Bueno-Rodríguez, L. Pérez-Villarejo, and D. Eliche-Quesada, "Reuse of Oil Refining Sludge Residue Ash via Alkaline Activation in Matrices of Chamotte or Rice Husk Ash," *Materials*, vol. 16, p. 2801, 2023, doi: 10.3390/ma16072801.

[56] J. Lin, Y. Zhang, and Z. Yang, "A Review of Recent Advances in Alkali-Activated Materials from Silica-Rich Wastes Derived Sodium Silicate Activators," *Journal of Advanced Concrete Technology*, vol. 21, pp. 189–203, 2023, doi: 10.3151/jact.21.189.

[57] X. Wan, L. Ren, T. Lv, D. Wang, and B. Wang, "Research on Alkali-Activated Systems Based on Solid Waste-Derived Activators: A Review," *Sustainability*, vol. 17, p. 254, 2025, doi: 10.3390/su17010254.

[58] C. Alvarado, D. Martínez-Cerna, and H. Alvarado-Quintana, "Geopolymer Made from Kaolin, Diatomite, and Rice Husk Ash for Ceiling Thermal Insulation," *Buildings*, vol. 14, no. 1, 2024, doi: 10.3390/buildings14010112.

[59] United Nations Environment Programme (UNEP), "Policy framework for circular economy in construction," 2023.

[60] International Energy Agency (IEA), "Global roadmap for low-carbon cement technologies," 2023. [Online]. Available: https://www.iea.org/reports/global-roadmap-for-low-carbon-cement-technologies

[61] ASTM International, “ASTM C230/C230M-23: Standard Specification for Flow Table for Use in Tests of Hydraulic Cement,” 2023.

[62] Bureau of Indian Standards, “IS 4031 (Part 6): 1988 — Methods of Physical Tests for Hydraulic Cement – Part 6: Determination of Compressive Strength of Hydraulic Cement (other than masonry cement),” 1988, *Bureau of Indian Standards, New Delhi, India*.

[63] ASTM International, “Standard Test Method for Compressive Strength of Hydraulic Cement Mortars (Using 2-in. or [50-mm] Cube Specimens),” 2023, *West Conshohocken, PA*.

[64] ASTM International, “ASTM C642-21 — Standard Test Method for Density, Absorption, and Voids in Hardened Concrete,” 2021, *ASTM International, West Conshohocken, PA, USA*. doi: 10.1520/C0642-21.

[65] E. M. Mulapeer and A. H. Omar, “Durability and Mechanical Performance of Geopolymer Mortar with RHA and Varying Activator Concentrations,” *Discover Civil Engineering*, 2025, doi: 10.1007/s44290-025-00234-8.

[66] Y. J. Patel and N. Shah, “Enhancement of the properties of Ground Granulated Blast Furnace Slag based Self Compacting Geopolymer Concrete by incorporating Rice Husk Ash,” *Constr Build Mater*, vol. 171, pp. 654–662, 2018, doi: 10.1016/j.conbuildmat.2018.03.166.

[67] C. Li, H. Sun, and L. Li, “A Review: Alkali-Activated Slag (Si+Ca) vs. Metakaolin (Si+Al) Cements,” *Cem Concr Res*, vol. 40, no. 9, pp. 1341–1349, 2010, doi: 10.1016/j.cemconres.2010.03.020.